

**APPENDIX I**  
**ROUND ROBIN ANALYSES**

## I.1 INTRODUCTION

As part of the BINP program, the program participants solved two separate round robin problems. Both problems formed the basis for subsequent technical tasks conducted by Battelle and Engineering Mechanics Corporation of Columbus (Emc<sup>2</sup>). The first round robin problem involved a series of finite element analyses aimed at developing a matrix of solutions to be used in quantifying the effect of restraint of pressure induced bending on the crack-opening displacements (COD) for leak-before-break (LBB) analyses. The results from this round robin problem then fed into Task 4 of the BINP program where the results from the round robin finite element analyses were curve fit to develop an engineering approximation of the effect of restraint of pressure induced bending on COD values.

The second round robin problem examined the effect of pipe radius-to-thickness (R/t) ratio on elastic-plastic fracture mechanics (EPFM) surface-crack J-estimation scheme analyses. The results from the second round robin then fed into Subtask 7.1 of the BINP program where the effect of R/t ratio on flaw evaluation criteria for Class 2, 3, and Balance of Plant (BOP) piping was studied.

This appendix provides the details of both round robins. The analysis methodologies that were developed in the subsequent BINP tasks are discussed elsewhere in this report.

## I.2 FIRST ROUND ROBIN (FINITE ELEMENT ANALYSIS OF CRACK-OPENING DISPLACEMENTS IN AXIALLY LOADED PIPING SYSTEMS FOR LEAK-BEFORE-BREAK APPLICATIONS)

At the end of the Second International Piping Integrity Research Group (IPIRG-2) Program, a study was commissioned to assess the factors that are most critical to leak-before-break (LBB) and in-service flaw evaluation methods (Ref. I.1). One such factor identified was an effect called *restraint of pressure induced bending on crack-opening displacements*. The existence of

a through-wall circumferential crack will result in a bending moment at the crack region for a pipe loaded axially, due to the eccentricity from the neutral axis of the crack plane versus the center of the uncracked pipe. The common analysis practice for LBB is to determine the center crack-opening displacement (COD) by using the solution for an end-capped vessel. The so-called end-capped vessel model, although relatively simple to analyze, allows the ends of the vessel to freely rotate. Furthermore, this model ignores the ovalization restraint at the crack plane from any boundary conditions. Therefore, the end-capped vessel model may over-estimate the crack-opening displacement more than if the pipe is not allowed to rotate.

In a real piping system, the ends of the pipe will be restrained from free rotation. The amount of the restraint will depend on the geometry of the pipe system. In general, the restraint of end rotation will be a function of:

- the magnitude of the load (elastic or plastic effects),
- the pipe R/t ratio,
- the length of the crack (short cracks typical of LBB in primary pipe loops are not affected, but long cracks for smaller-diameter pipe will be effected), and
- the boundary conditions of the pipe either side of the crack location.

For this round robin, six organizations from three countries participated in the finite element round-robin analysis. The objective of this round-robin program was to check the past calculations (Ref. I.1), as well as compare and evaluate the results and modeling approaches from different participants. Each participant was then assigned to solve some additional problems. This resulted in a large matrix of FE results, which would lend themselves to a closed-form analytic expression that was developed later in the BINP program.

The round robin analysis was coordinated by Engineering Mechanics Corporation of Columbus (Emc<sup>2</sup>). The other five participating organizations were: Battelle Columbus, Central Research Institute of Electric Power Industry (CRIEPI) of Japan, Korea Electric Power Research Institute (KEPRI), Sungkyunkwan University of Korea (SKKU), and the U.S. Nuclear Regulatory Commission (NRC).

### **I.2.1 Background on the Effect of Pipe-System Boundary Conditions on Fracture and Leak Rate Analyses**

In virtually all nuclear pipe fracture analyses, the pipe-system stress analysis and the fracture analyses are decoupled. That is, typically the stresses in an uncracked-pipe system are determined, and then those stresses are used in an analytical fracture analysis.

Of the effects that are typically decoupled, one of the most stunning results observed came from a pipe-system experiment in the First International Piping Integrity Research Group (IPIRG-1) program. In that experiment, it was experimentally determined that a guillotine break did not occur until the growing through-wall crack was 95 percent around the pipe circumference, see Figure I.1. From pressure loads alone, it was expected that a break would occur once the crack reached 65 percent of the circumference. The crack length of 95-percent of the circumference corresponded to the pressure-induced failure for full restraint of the induced bending moment, see Figure I.2.

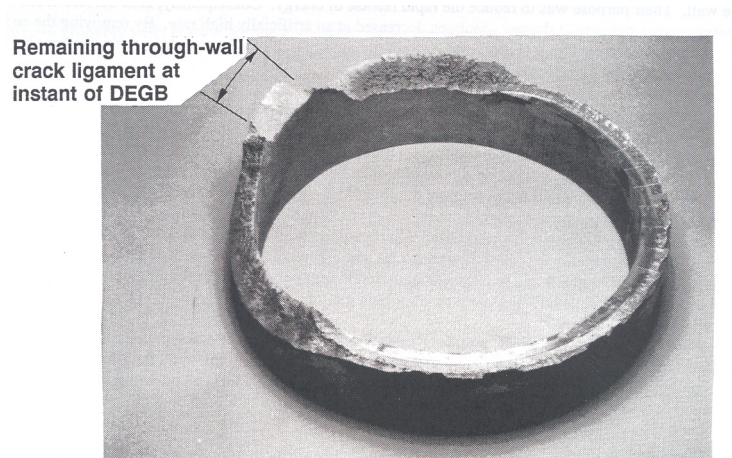


**Figure I.1 Photograph of fracture from aged cast stainless experiment (Experiment 1.3-7) from IPIRG-1**

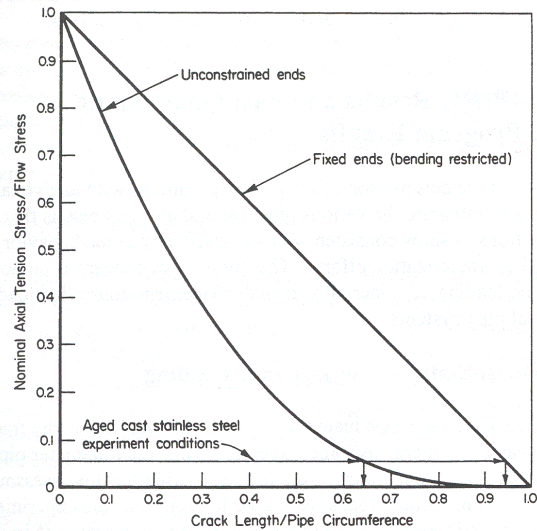


**Figure I.2 Net-Section-Collapse analyses predictions, with and without considering induced bending, as a function of the ratio of the through-wall crack length to pipe circumference**

The results from this experiment, with the crack located 3.4 pipe diameters from an elbow, provide strong evidence that pipe-system boundary conditions restrain pressure-induced bending, and that this increases the load-carrying capacity of the cracked pipe. Virtually all fracture analyses assume that the pipe is free to rotate due to the pressure-induced bending.

Consequently, the contemporary fracture methods will tend to inaccurately predict the propensity for crack instability because they ignore the restraint that pipe-system boundary conditions provide.

After the excitement subsided concerning the apparent beneficial effects of the restraint of pressure-induced bending on fracture loads, it was later noted, that if the failure loads are increased, then the driving force is reduced, so that the crack-opening displacement in the pipe system will be less than what is typically calculated using current crack-opening-

displacement analyses. Hence, the increased load-carrying capacity that is beneficial to LBB is offset by a corresponding decrease in crack-opening displacement that is detrimental to LBB. Because the trade-offs between these two effects were not well understood, some selected case studies were undertaken which are summarized below.

The precise procedure that was originally used by Battelle to assess the effects of restraining the induced bending from pressure loads was defined in NUREG/CR-6300, Section 6.3 on page 6-3 (Ref. I.2). A focused mesh was used at the circumferential crack tip with 20-noded brick elements in ABAQUS. There were 172 elements in the quarter symmetry model with 1,252 nodes, as shown in Figure I.3. Calculations were initially done for a 28-inch diameter pipe with a mean pipe radius to wall thickness ratio (R/t) of 10. Only elastic analyses were conducted.

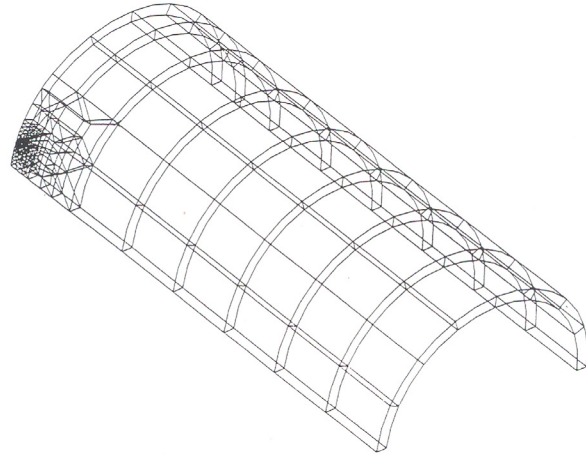


**Figure I.3 FE mesh used in past Battelle COD/Restraint effect study**

At various distances from the circumferential crack plane, the pipe rotations and ovalizations were restricted in the FE analyses. This distance from the crack to the restraining boundary conditions was called the restraint length. The restraint length was normalized by the pipe diameter for making non-dimensional plots with COD values for different pipe diameters.

In NUREG/CR-6300, the crack length was either 12.5 or 25 percent of the pipe

circumference, and the normalized restraint length was 1, 5, 10, and 20. A calculation was also done that would allow free rotation and no ovalization restrictions. This is representative of the fully unrestrained conditions (the end-capped vessel assumption) typically used in all the COD estimation procedures. Since this was an elastic analysis, the COD of the restrained boundary condition analyses could be normalized by the unrestrained COD for any load level. Figure I.4 shows the initial results.

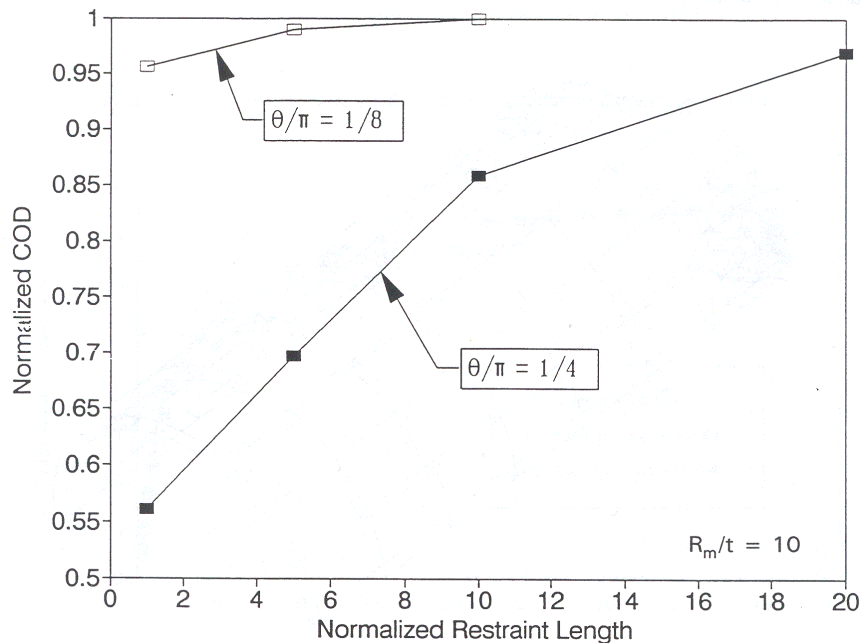


**Figure I.4 Normalized graph showing the effects of restraining ovalization and rotations at different distances from the crack plane**

Subsequent analyses were conducted for a 4-inch nominal diameter pipe with an R/t of 6. In addition, another crack length of ½ of the pipe circumference (total crack length) was added for both pipe diameters. Figure I.5 shows the results of the both of these analyses together.

The results from the 28-inch diameter pipe FE analysis seem reasonable. The 4-inch nominal diameter pipe results agree with the large pipe results for the large crack, but not for the small or intermediate crack. That may have been due to some problem in the normalization. One would think that the normalized COD should flatten off to a constant value of 1.0. Hence, the small-diameter results are suspicious.

An additional LBB sensitivity study was conducted in NUREG/CR-6443 using the above restrained COD trends. The LBB analysis used the mesh geometry shown in Figure I.3, for a highly restrained condition (L/D = 1) and completely unrestrained conditions applied to 4-inch nominal diameter (R/t of 6) and 28-inch (R/t of 10) diameter pipes under the following conditions:

- a leak rate of 1.89 liters/min (0.5 gpm),

- IGSCC crack morphology parameters,
- a pressure of 15.5 MPa (2,250 psi), and
- a bending stress chosen to give a total pressure plus bending stress of 50-percent of the Service Level A maximum allowable stress from ASME Section III Article NB-3650 for TP304 pipe.

The resulting leakage-size crack was calculated using the SQUIRT Version 2.4 computer code. These results are shown in Table I.1. At this leak rate, the large-diameter pipe is basically unaffected by the restraint condition while the small-diameter pipe is very much affected. The effect of restraint on the COD is strongly controlled by the crack length. It appears to manifest itself as a pipe diameter effect, since a longer normalized crack length is needed in smaller-diameter pipe for LBB to be satisfied.

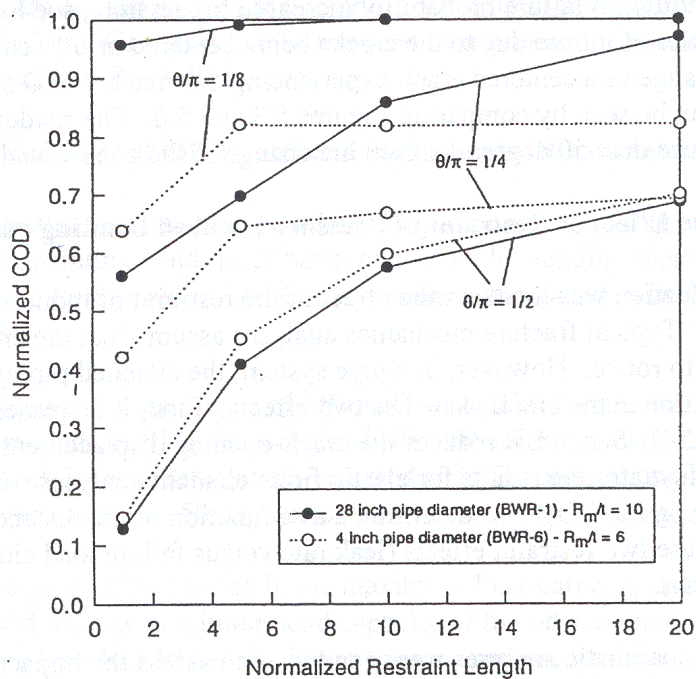


Figure I.5 Normalized COD versus restraint length for two different sets for FE analyses

**Table I.1 Differences in leakage flow sizes due to restraint of pressure-induced bending**

Outside Pipe Diameter		Leakage Crack Length, $\theta/\pi$	
Mm	inches	Restrained	Unrestrained
114.3	4.5	0.7250	0.2360
711.2	28.0	0.0219	0.0219

The corresponding LBB fracture loads were evaluated under the following conditions:

- the crack is centered on the bending plane,
- the average stress-strain curve properties for TP304 stainless steel base metal were used, and
- the crack was assumed to be in the center of the weld, hence the mean minus one standard deviation J-R curve for a stainless steel SAW weld was used.

Using the LBB.ENG2 analysis modified to eliminate the induced bending from the tension component of the axial stress component, the ratio of the unrestrained to restrained failures loads is shown in Figure I.6. This result shows that the effects of the restraint of pipe-system boundary conditions were negligible for the 28-inch diameter pipe. This was because for this leak rate, the crack size was a small percent of the circumference, and hence the beneficial effects on fracture and detrimental effects on COD were negligible. However, the effect on the 4-inch nominal diameter pipe was very large. The unrestrained load is a factor of nine larger than the restrained load. This was a more significant effect than any possible effect from toughness considerations. The reason this occurred was that for this leak rate, under this

loading, the normalized crack length in the small pipe for the restrained condition had to be very large when compared with the larger-diameter pipe. The crack, in fact, became so large from this effect, that any benefits on fracture loads were small, especially considering that the additional loads to fracture were all bending loads, not increases in pressure loads. Also, like any LBB analysis, the calculations were made up to maximum load, and were not an actual determination of a DEGB.

The effect seen in this sample calculation suggests that LBB applications need to be assessed carefully for cases where large crack sizes may occur, i.e., small-diameter pipe, or steam-line applications. It also suggests that there may be some concern with LBB applications to intermediate pipe diameters. Fortunately, for large-diameter pipe, where LBB is of greatest benefit, there are no detrimental effects from this phenomenon.

Of practical importance is the fact that the past Battelle analysis assumes symmetric boundary conditions either side of the crack. This would probably never occur in practice. Hence, to make any analysis for this effect a practical tool, one would have to account for the different pipe bending stiffnesses on either side of the proposed crack locations.

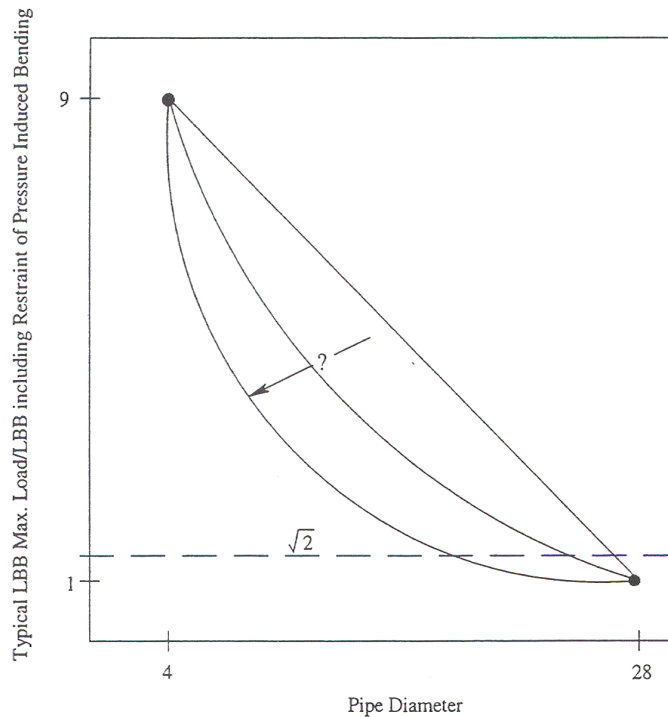


**Figure I.6 Calculated maximum loads for LBB with and without restraint of the pressure-induced bending from the pipe system**

### I.2.2 Problem Statement for First Round Robin Analyses

The objective of this round robin was for the participants to perform linear-elastic finite element analysis to determine the center crack-opening displacement (COD) at the mid-thickness of a through-wall circumferentially-cracked straight pipe restrained at both ends (Figure I.7). The elastic modulus and the Poisson's ratio were assumed to be 200 GPA (29,000 ksi) and 0.3, respectively. The basic variables investigated in the program included the pipe outside diameter (*OD*), pipe mean radius to thickness ratio ( $R_m/t$ ), half crack length ( $\theta$ ), and the distance between the restraint planes to the crack plane ( $L_1, L_2$ ).

A total of 144 cases were included in the analysis matrix of the round robin. It covered a wide range of pipe diameters and  $R_m/t$  ratios. The effects of different restraint lengths on the two sides of a crack plane (the asymmetric restraint condition) were considered also. The

analysis matrix included the cases that were analyzed in NUREG/CR-6300 to evaluate the validity of the prior calculations.

The specifics of each case in the analysis matrix are provided in Table I.2 and Table I.3. The analysis matrix was grouped into three major case groups, namely, Case 1, Case 2 and Case 3. Case 1 considered the symmetrically restrained pipe with constant  $R_m/t$  ratio of 10, but varying pipe diameters. Case 2 was also the symmetric restraint case, but with a constant pipe diameter of 28 inches and varying  $R_m/t$  ratios. Case 3 covered the asymmetric restraint case, with a  $R_m/t$  ratio of 10 and varying pipe diameters.

Furthermore, the round robin was carried out into two phases. In the first phase all of the participants were required to solve all the cases in Case 1. The modeling approach and COD results from each participant were compared. In the subsequent phase (Phase II), the participants were assigned to solve a different subset of cases in Case 2 and Case 3. This resulted in a COD

database that would be used to develop a closed-form analytical expression in one of the follow-on tasks of the BINP program. Table I.4

summarizes the cases solved by each participant of the program.

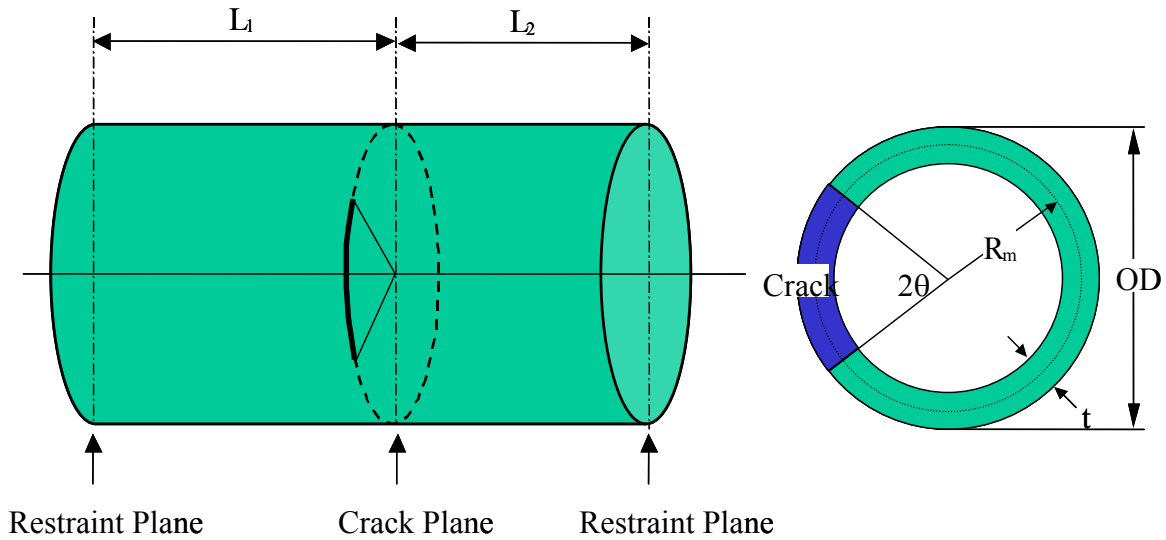


Figure I.7 Cracked-pipe geometry

Table I.2 Symmetric restraint cases

	OD (mm)	$R_m/t$	Axial Force (kN)	Half Crack Length (radians)			Restraint Length (L/OD)			
				$\pi/8$	$\pi/4$	$\pi/2$	1	5	10	20
Case 1a	711.2	10	50,000	$\pi/8$	$\pi/4$	$\pi/2$	1	5	10	20
Case 1b	323.85	10	5,000	$\pi/8$	$\pi/4$	$\pi/2$	1	5	10	20
Case 1c	114.3	10	500	$\pi/8$	$\pi/4$	$\pi/2$	1	5	10	20
Case 2a	711.2	5	50,000	$\pi/8$	$\pi/4$	$\pi/2$	1	5	10	20
Case 2b	711.2	20	50,000	$\pi/8$	$\pi/4$	$\pi/2$	1	5	10	20
Case 2c	711.2	40	50,000	$\pi/8$	$\pi/4$	$\pi/2$	1	5	10	20

Table I.3 Asymmetric restraint cases

	OD (mm)	$R_m/t$	Axial Force (kN)	Half Crack Length (radians)			Restraint Length (L <sub>1</sub> /OD)			L <sub>2</sub> /OD
				$\pi/8$	$\pi/4$	$\pi/2$	5	10	20	
Case 3a	711.2	10	50,000	$\pi/8$	$\pi/4$	$\pi/2$	X	X	X	1
	711.2	10	50,000	$\pi/8$	$\pi/4$	$\pi/2$		X	X	5
	711.2	10	50,000	$\pi/8$	$\pi/4$	$\pi/2$			X	10
Case 3b	323.85	10	5,000	$\pi/8$	$\pi/4$	$\pi/2$	X	X	X	1
	323.85	10	5,000	$\pi/8$	$\pi/4$	$\pi/2$		X	X	5
	323.85	10	5,000	$\pi/8$	$\pi/4$	$\pi/2$			X	10
Case 3c	114.3	10	500	$\pi/8$	$\pi/4$	$\pi/2$	X	X	X	1
	114.3	10	500	$\pi/8$	$\pi/4$	$\pi/2$		X	X	5
	114.3	10	500	$\pi/8$	$\pi/4$	$\pi/2$			X	10

**Table I.4 Problems analyzed by the participants**

	Participant A	Participant B	Participant C	Participant D	Participant E	Participant F
Case 1a	X	Partial	X	X	X	X
Case 1b	X	X	X	X	X	X
Case 1c	X		X	X	X	X
Case 2a						X
Case 2b					X	
Case 2c			X	X		
Case 3a						X
Case 3b		X			X	
Case 3c			X	X		

It should be noted that, although the problem statement was very specific about other aspects of the problem, it deliberately avoided stipulating how the restraint conditions in a pipe system and the axial load should be applied in the finite element model. This reflects the complex nature of the restraint conditions in various piping systems. The round-robin participants would have to decide on how the restraint and loading conditions would be imposed in their finite element models according to their own interpretations of the piping system. Indeed, different participants imposed the boundary and loading conditions differently, which might be one of the causes for the observed discrepancies of the COD results in the round-robin cases.

The problem statement as distributed to all participants is given below.

***Case 1 – Common Problems – All Participants***

**Case 1a Problem Statement**

Using elastic FEM analyses (brick or thick-shell element), calculate the COD at the center of a circumferential through-wall-cracked pipe using the following input parameters:

- Outside diameter of 28-inch,
- The model can be quarter symmetry to give symmetric boundary conditions either side of the crack, see Figure I.3,

- At the crack plane, allow the pipe to move vertically and horizontally (rotation in the crack plane and ovalization are not restricted), but pin any axial displacements in the ligament,
- Do not apply pressure on the crack faces, and no internal pressure,
- Apply an axial force of 50,000 kN, (11,240 pounds)<sup>(1)</sup> through the center of the uncracked pipe at the end of the model,
- The mean-radius to thickness ratio is 10,
- The total crack lengths (2θ) are 12.5, 25, and 50 percent of the pipe circumference,
- The distances from the crack to the plane of rotation and ovalization restraint should be 1, 5, 10, and 20 outside diameters of the pipe, as well as, unrestrained rotation and ovalization conditions (capped pressure vessel case) for each crack length.

This should be a matrix of 15 FE analyses, where the COD can be given in a table, as well as plotted in a normalized fashion as in Figure I.4.

---

<sup>1</sup> The applied load value is arbitrarily selected since the analysis is linear elastic and will be normalized for restrained versus unrestrained COD values.

### **Case 1b Problem Statement – all participants**

This is similar to Case 1a, but uses a 12-inch nominal diameter pipe with an  $R_m/t$  of 10.

This should also result in a matrix of 15 FE analyses, where the COD can be given in a table, as well as plotted in a normalized fashion as in Figure I.4.

### **Case 1c Problem Statement – all participants**

This is a similar problem, but for the 4-inch nominal diameter pipe case shown in Figure I.5.

Again, this should be a matrix of 15 FE analyses, where the COD can be given in a table, as well as plotted in a normalized fashion as in Figure I.4.

### **Case 2 – Different $R_m/t$ Cases**

#### **Case 2a Problem Statement – Selected Participants**

Repeat the analysis for Case 1a, but use an  $R_m/t$  ratio of 5.

#### **Case 2b Problem Statement – Selected Participants**

Repeat the analysis for Case 1a, but use an  $R_m/t$  ratio of 20.

#### **Case 2c Problem Statement – Selected Participants**

Repeat the analysis for Case 1a, but use an  $R_m/t$  ratio of 40.

### **Case 3 – Nonsymmetrical Restraint Length Cases**

#### **Case 3a Problem Statement – Selected Participants**

Repeat the analysis for Case 1a for the 28-inch diameter pipe with an  $R_m/t$  of 10, but use the following nonsymmetrical restraint lengths. (Half-symmetry pipe FE model needed in these cases.)

1. Restraint length on one side of the crack is equal to one pipe diameter, and the restraint length on the other side of the crack is 5, 10, and 20 pipe diameters from the crack plane.
2. Restraint length on one side of the crack is equal to 5 pipe diameters, and the restraint length on the other side of the crack is 10 and 20 pipe diameters from the crack plane.
3. Restraint length on one side of the crack is equal to 10 pipe diameters, and the restraint length on the other side of the crack is 20 pipe diameters from the crack plane.

This involves six FE calculations for each of the three crack lengths for a total of 18 FE solutions. COD values were to be provided in a table, and normalized by the unrestrained COD values from Case 1a.

#### **Case 3b Problem Statement – Selected Participants**

Repeat the analysis for Case 1b for the 12.75-inch diameter pipe with an  $R_m/t$  of 10, and using the same nonsymmetrical restraint lengths as for Case 3a. (Again, half-symmetry pipe FE models are needed in these cases.)

This involves six FE calculations for each of the three crack lengths for a total of 18 FE solutions. COD values were to be provided in a table, and normalized by the unrestrained COD values from Case 1b.

#### **Case 3c Problem Statement – Selected Participants**

Repeat the analysis for Case 1c for the 4.5-inch outside diameter pipe with an  $R_m/t$  of 10, and using the same nonsymmetrical restraint lengths as for Cases 3a and 3b. (Again, half-symmetry pipe FE model are needed in these cases.)

This involves six FE calculations for each of the three crack lengths for a total of 18 FE solutions. COD values were to be provided in a table, and normalized by the unrestrained COD values from Case 1c.

### I.2.3 Modeling Approaches

This section compiles the finite element modeling approaches adapted by each of the round-robin participants. The readers should consider the differences in the modeling approaches when comparing the results from all participants.

**I.2.3.1 Participant A** - As shown in Table I.4, Participant A only participated in the common round-robin cases (i.e., Case 1). Participant A modeled the pipe using 3D 20-node second-order solid-brick elements. All the meshes and models were created using FEMAP Version 6.0, and solved with ABAQUS Version 5.8. Figure I.8 is a hidden view of a typical finite element mesh. One layer of elements was used through the pipe thickness. A regular mesh, refined

around the crack tip, was used to discretize the crack-tip region.

At the restrained end of the pipe, the TIE option of the multipoint constraint (MPC) feature in ABAQUS was used to make all corresponding degrees of freedom of the nodes at the restraint plane equal to those of an extra node on the axis of the pipe. This extra node was used for applying a concentrated force in the axial direction as specified in the problem statement. Tables I.5 through Table I.7 summarize the number of elements and nodes used in each of the cases analyzed by Participant A. Notice that the numbers of elements and nodes increase as the restraint length increases. This is due to the fact that the length of the pipe in the finite element model was set to be same as the restraint length.

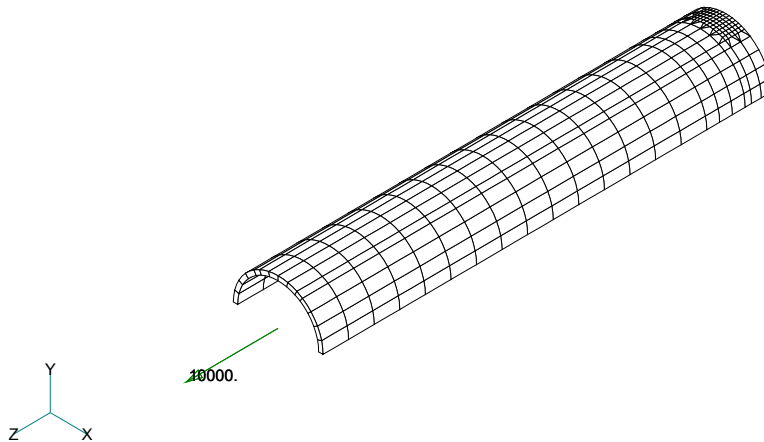


**Figure I.8** Representative finite element mesh used by Participant A

Table I.5 Matrix of FE runs by Participant A – Case 1a

Job ID	Half Crack Length	L/D	Constrained	Number Of Nodes	Number Of Elements	Round Robin Case
Pipe3d	$\pi/2$	1	Yes	1334	178	Case 1a
Pipe3d1	$\pi/2$	5	Yes	2776	374	Case 1a
Pipe3d2	$\pi/2$	10	Yes	4630	626	Case 1a
Pipe3d3	$\pi/2$	20	Yes	8235	1116	Case 1a
Pipe3d4	$\pi/2$	20	No	8235	1116	Case 1a
Pipe3dx	$\pi/4$	1	Yes	1334	178	Case 1a
Pipe3dx1	$\pi/4$	5	Yes	2776	374	Case 1a
Pipe3dx2	$\pi/4$	10	Yes	4630	626	Case 1a
Pipe3dx3	$\pi/4$	20	Yes	8235	1116	Case 1a
Pipe3dx4	$\pi/4$	20	No	8235	1116	Case 1a
Pipe3dy	$\pi/8$	1	Yes	1278	167	Case 1a
Pipe3dy1	$\pi/8$	5	Yes	2719	363	Case 1a
Pipe3dy2	$\pi/8$	10	Yes	4573	615	Case 1a
Pipe3dy3	$\pi/8$	20	Yes	8179	1178	Case 1a
Pipe3dy4	$\pi/8$	20	No	8179	1178	Case 1a

Table I.6 Matrix of FE runs by Participant A – Case 1b

Job ID	Half Crack Length	L/D	Constrained	Number Of Nodes	Number Of Elements	Round Robin Case
12Pipe3d	$\pi/2$	1	Yes	1334	178	Case 1b
12Pipe3d1	$\pi/2$	5	Yes	2776	374	Case 1b
12Pipe3d2	$\pi/2$	10	Yes	4630	626	Case 1b
12Pipe3d3	$\pi/2$	20	Yes	8235	1116	Case 1b
12Pipe3d4	$\pi/2$	20	No	8235	1116	Case 1b
12Pipe3dx	$\pi/4$	1	Yes	1334	178	Case 1b
12Pipe3dx1	$\pi/4$	5	Yes	2776	374	Case 1b
12Pipe3dx2	$\pi/4$	10	Yes	4630	626	Case 1b
12Pipe3dx3	$\pi/4$	20	Yes	8235	1116	Case 1b
12Pipe3dx4	$\pi/4$	20	No	8235	1116	Case 1b
12Pipe3dy	$\pi/8$	1	Yes	1278	167	Case 1b
12Pipe3dy1	$\pi/8$	5	Yes	2719	363	Case 1b
12Pipe3dy2	$\pi/8$	10	Yes	4573	615	Case 1b
12Pipe3dy3	$\pi/8$	20	Yes	8179	1178	Case 1b
12Pipe3dy4	$\pi/8$	20	No	8179	1178	Case 1b

Table I.7 Matrix of FE runs by Participant A – Case 1c

Job ID	Half Crack Length	L/D	Constrained	Number Of Nodes	Number Of Elements	Round Robin Case
4Pipe3d	$\pi/2$	1	Yes	1334	178	Case 1c
4Pipe3d1	$\pi/2$	5	Yes	2776	374	Case 1c
4Pipe3d2	$\pi/2$	10	Yes	4630	626	Case 1c
4Pipe3d3	$\pi/2$	20	Yes	8235	1116	Case 1c
4Pipe3d4	$\pi/2$	20	No	8235	1116	Case 1c
4Pipe3dx	$\pi/4$	1	Yes	1334	178	Case 1c
4Pipe3dx1	$\pi/4$	5	Yes	2776	374	Case 1c
4Pipe3dx2	$\pi/4$	10	Yes	4630	626	Case 1c
4Pipe3dx3	$\pi/4$	20	Yes	8235	1116	Case 1c
4Pipe3dx4	$\pi/4$	20	No	8235	1116	Case 1c
4Pipe3dy	$\pi/8$	1	Yes	1278	167	Case 1c
4Pipe3dy1	$\pi/8$	5	Yes	2719	363	Case 1c
4Pipe3dy2	$\pi/8$	10	Yes	4573	615	Case 1c
4Pipe3dy3	$\pi/8$	20	Yes	8179	1178	Case 1c
4Pipe3dy4	$\pi/8$	20	No	8179	1178	Case 1c

**I.2.3.2 Participant B** - Participant B solved Case 1a (except for the case of L/D=5), Case 1b, and Case 3b. The finite element code used by Participant B was ABAQUS.

For the symmetrically restrained cases, a quarter symmetry model with 776 elements and 4,641 nodes was applied. Regardless of the restraint length, the same FE model with a pipe length of  $30D_m$  (pipe mean diameter) was used. Only the location to apply the load and the boundary condition were changed in accordance with the restraint lengths specified for each problem.

For the cases of the asymmetric restraint length, a half symmetry model with 1,160 elements and 6,897 nodes was applied. Similar to the symmetric restraint cases, a single FE model with a pipe length of  $50D_m$  was used.

For all the cases, two layers of elements were used for pipe thickness. The crack tip region was discretized with a focused mesh. The 20-noded second-order brick elements were used. Figure I.9 and Figure I.10 show the finite element meshes for the symmetric restraint

length and asymmetric restraint length cases, respectively.

The axial load was applied on the cross-section plane at a distance equal to the restraint length from the cracked plane as a uniform tensile stress calculated from the axial force.

**Boundary conditions for the unrestraint cases**

In the symmetric restraint model, the z-directional symmetry boundary condition was applied to all nodes in the crack ligament and the y-directional displacement at a node on the center of the crack ligament was fixed to prevent the free body motion.

In the asymmetric restraint model, a node on the center of the crack ligament was fixed in the y and z directions to prevent the free body motion. In addition, the tensile stresses were applied on the two planes at the respective restraint lengths from the crack plane.

In both models, the rotations induced by applied axial load was allowed.

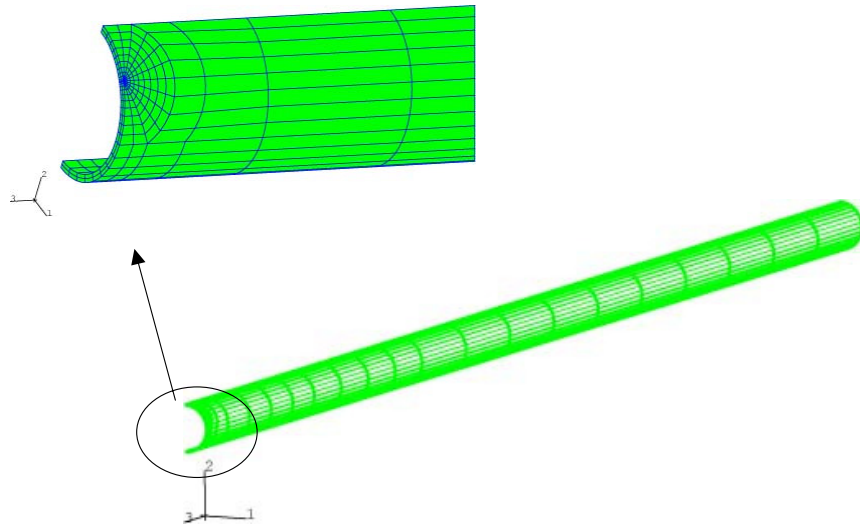


**Figure I.9** Finite element mesh used by Participant B for symmetric restraint cases

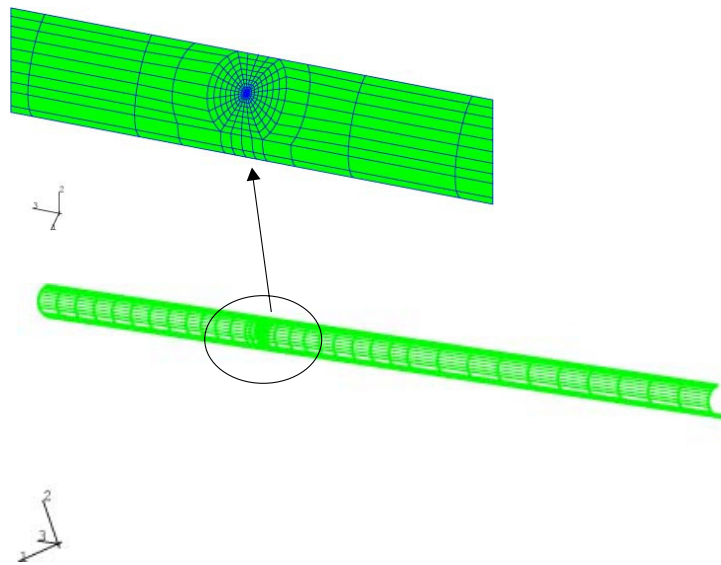


**Figure I.10** Finite element mesh used by Participant B for asymmetric restraint cases

**Boundary conditions for the restraint cases**

The restraint to pressure-induced bending was simulated by constraining the movement in both

the radial and circumferential directions, but allowing for the axial movement, for all the nodes beyond the restraint lengths. This is shown in Figure I.11 and Figure I.12.

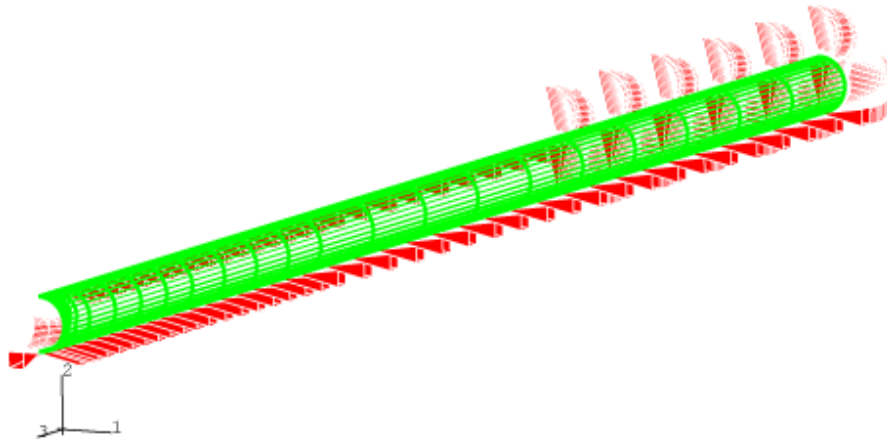


**Figure I.11** Boundary conditions for restraining the bending induced tension in the symmetric FE model



**Figure I.12** Boundary conditions for restraining the bending induced tension in the asymmetric FE model

**I.2.3.3 Participant C** – Participant C used ABAQUS Version 5.8-14 for the COD calculations. 20-noded second-order solid brick elements with reduced integration (ABAQUS element type C3D20R) were used. The pipe length was set to the restraint length for the symmetric restraint cases (quarter-symmetrical model), and the sum of the two restraint lengths for the asymmetric restraint cases (half-symmetrical model). For the unrestraint cases, the length of the pipe was set to  $20D_m$ . Additional analyses were also performed with pipe lengths up to  $100D_m$  to evaluate the effect of pipe length on the unrestraint CODs.

The prescribed axial load was imposed using the “Distributing Coupling Element” feature in ABAQUS as shown in Figure I.13. The distributing coupling element ties all the nodes at the end of the pipe to a single-noded coupling

element (Node 1 in Figure I.13) located on the axis of the pipe. The total axial force is applied through the coupling element that then distributes the load to the end of the pipe.

To simulate the pipe restraint effects, the end of the pipe is fixed against the radial and circumferential movement, while allowing for the axial movement. This is shown in Figure I.14 and Figure I.15, respectively, for the symmetric, and asymmetric restraint length cases, respectively.

Figure I.16 shows the axial stress and displacement distributions obtained with the distributing coupling element. It clearly shows that, although the displacement is relatively uniform, the stress varies significantly at the restraint plane.

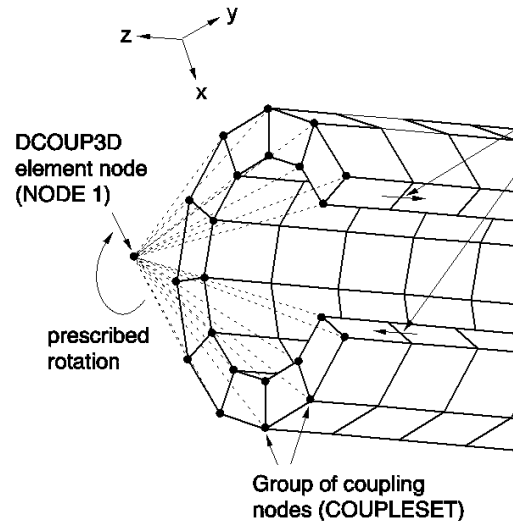


**Figure I.13** The “Distributing Coupling Element” in ABAQUS

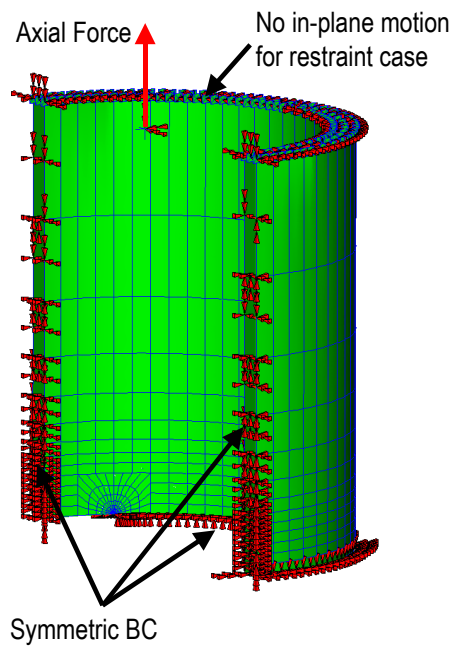


**Figure I.14** The finite element mesh and associated boundary conditions used by Participant C for the symmetric restraint cases

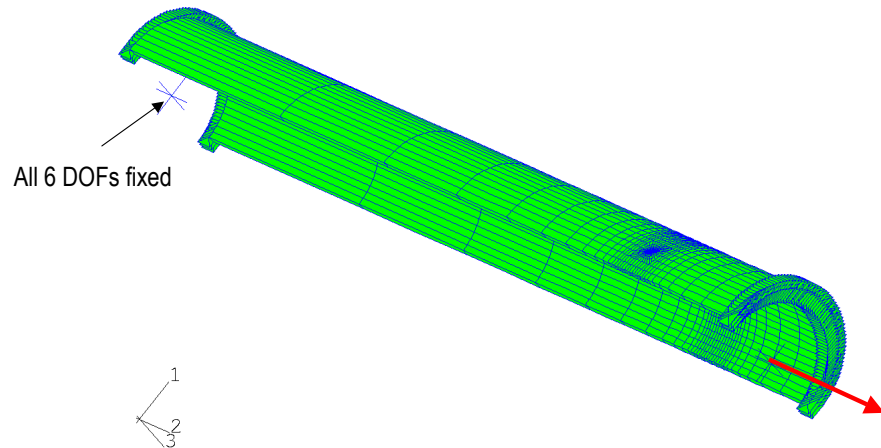


**Figure I.15** The finite element mesh and associated boundary conditions used by Participant C for the asymmetric restraint cases

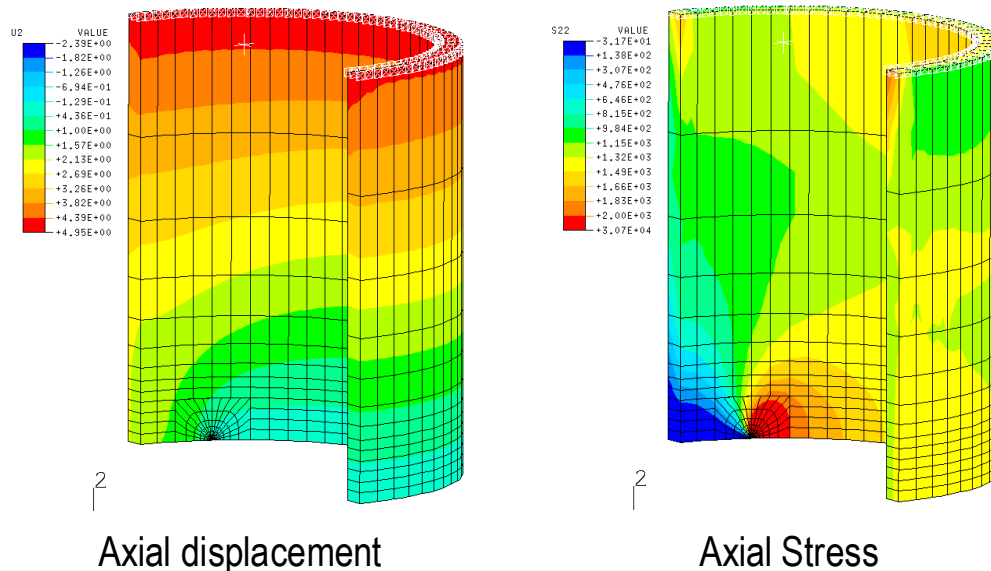


**Figure I.16** Axial displacement and stress distributions using the distributing coupling element to impose the axial load (Case 1a,  $L/D=1$ ,  $\theta/\pi=1/8$ , Participant C)

**I.2.3.4 Participant D** - Participant D used ABAQUS Version 5.8-17 to solve all the cases. 8-noded first-order solid-brick elements with reduced integration (ABAQUS element type C3D8R) were used to discretize the pipe. The number of element layers along the pipe thickness was one. Since there was no node at the mid-thickness, the COD was calculated by averaging the displacements of the nodes on the inner and outer surfaces of the pipe at the crack center.

Similar to Participant B, the pipe length in the

finite element model was the same for all the cases analyzed, which is 20D for the symmetric cases, and 30D for the asymmetric cases. The restraint length effect was treated by changing the boundary conditions such that the restrained section of the pipe only allowed for the axial displacement.

Figure I.17 shows the finite element mesh used by Participant D. Focused mesh was not used. The pipe was meshed out evenly in the circumferential direction, but with a finer

element length in the axial direction at the cracked section.

The axial load was applied to the end of the pipe as a uniform tension stress calculated from the axial force.

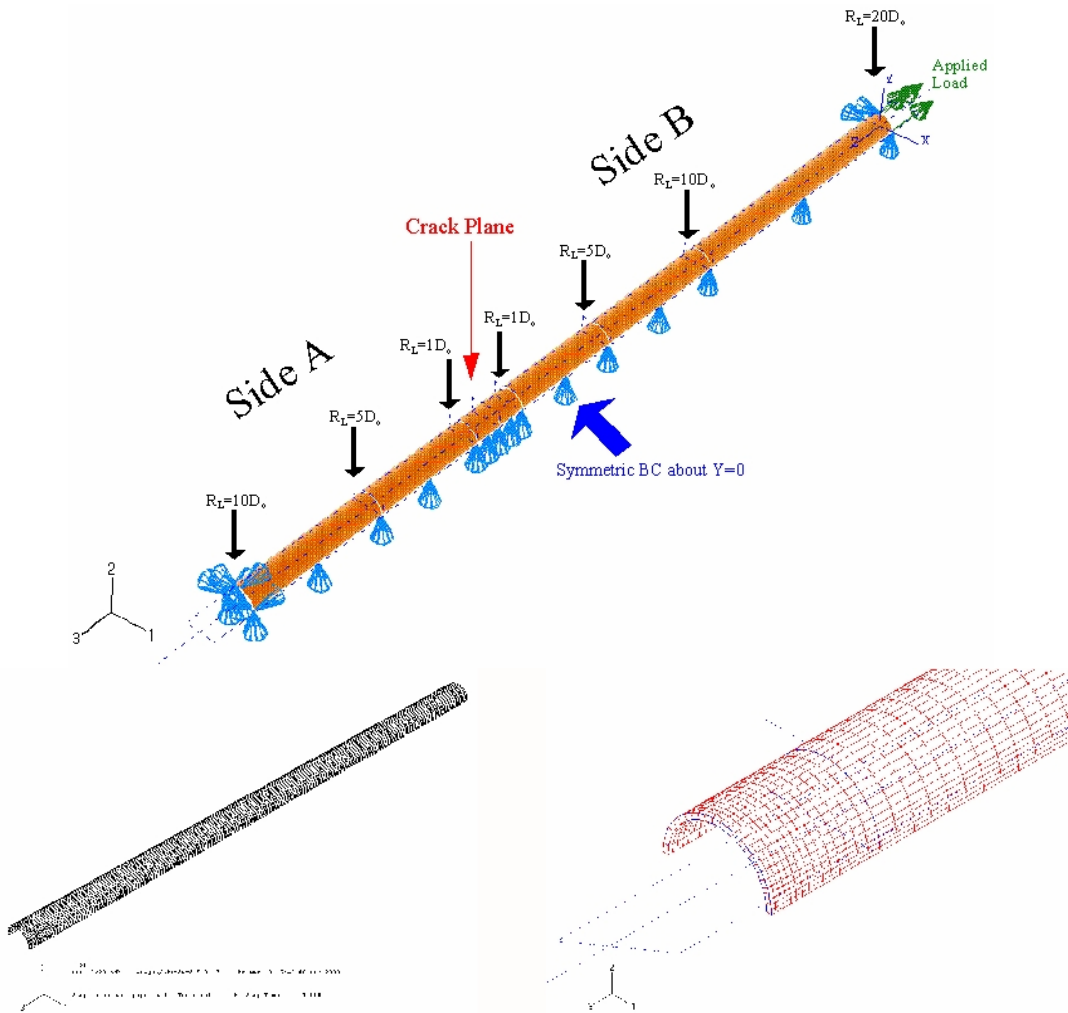


**Figure I.17 Boundary conditions and mesh used by Participant D**

**I.2.3.5 Participant E** - Participant E followed the basic steps as described in the NUREG/CR-6300 report, which were:

- Step 1: Create a finite element model of a cracked pipe with a total pipe length of twice the restraint length.
- Step 2: Apply an arbitrary positive (tensile) displacement loading,  $\Delta$ , in the axial direction of the pipe to all the nodes in the cross section located at a distance  $L_R$  from the cracked plane.

Step 3: Conduct a finite element analysis and determine the COD resulting from the remote displacement,  $\Delta$ . The stresses at the cross section A-A are not uniform and can be decomposed into a bending component and a tensile component. Denote the COD (unscaled) and the tension stress by  $\delta_{uns}$  and  $\sigma_{ten}$ , respectively.

Step 4: Compute the scaled COD,  $\delta_s = \delta_{uns} \times (\sigma_{ref} / \sigma_{ten})$ , where  $\sigma_{ref}$  is reference tensile stress.

Step 5: In the same finite element model apply a

tension stress loading of magnitude  $\sigma_{ref}$  but allowing free rotation. Denote the resultant COD by  $\delta_{\infty}$ .

- Step 6: Divide the scaled COD,  $\delta_s$ , by the reference COD,  $\delta_{\infty}$ , to get the normalized COD,  $\delta_{NOR} = \delta_s / \delta_{\infty}$ .
- Step 7: For a given crack geometry, repeat Steps 1-6 for several values of  $L_R$ . Develop a plot of  $\delta_{NOR}$  versus  $L_R / D_m$  and hence, determine the effects of the normalized restraint length,  $L_R / D_m$  on the COD.

Figure I.18 shows a typical mesh design for the symmetric restraint case. Linear elastic finite element analyses were performed using the 20-noded 3D brick elements in ABAQUS. A focused mesh was used at the crack tip. The total number of elements was 936. Two layers of elements were used through the thickness. Considering the symmetric condition, only one quarter of the pipe was modeled. The arbitrary applied axial displacement,  $\Delta$ , was set equal to 2.54 mm (0.1 inches) (Step 2). The applied displacement was applied through a MPC (multi-point constraint in ABAQUS) at the end of the pipe (allow free rotation and no ovalization restrictions). The COD values were estimated at the mean thickness of the center of the crack.

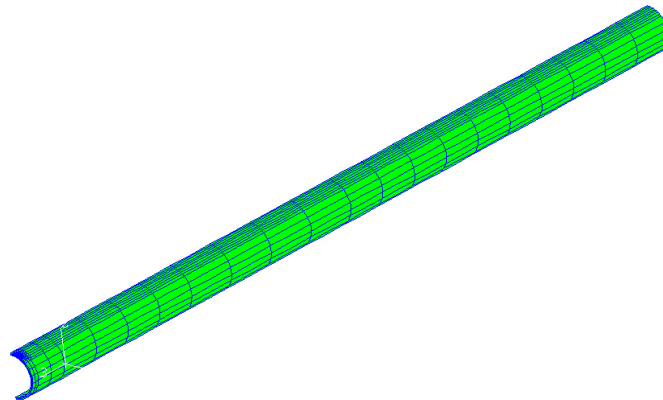


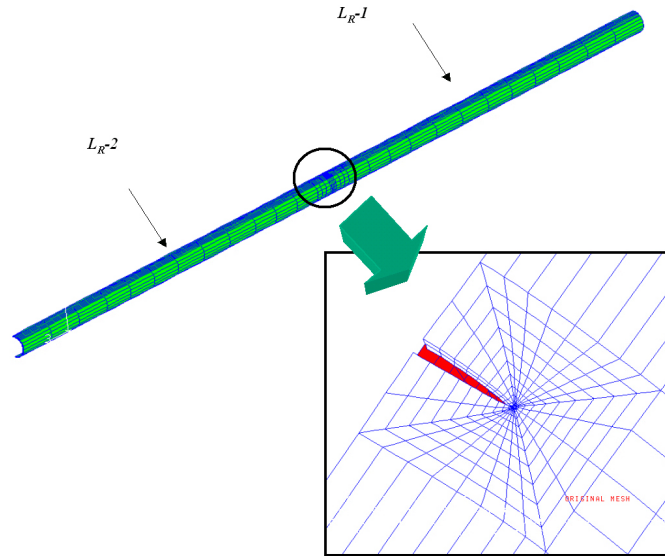
Figure I.18 Typical finite element mesh for the symmetric case by Participant E

Figure I.19 shows a typical mesh for the asymmetric case, which is a half symmetric FE model. A focused mesh was also used at the crack tip. The total number of elements was 1,552. All displacements and rotations were fixed at one end of the pipe (the right end in Figure I.19), while the other end was subjected to the given applied axial displacement. The COD values were normalized by the unrestrained COD values from Case 1b.

**I.2.3.6 Participant F** – Participant F calculated the COD values using MARC, a commercial finite element package. 20-noded 3D solid brick elements were used, with a focused mesh near the crack tip. The number of element layers along the pipe thickness was one.

On the restrained section, all the nodes were tied to the node where the rotation around all three axes was fixed (see Figure I.20), so that all the nodes on the restraint plane remained plane during loading. The concentrated axial load was then applied to the tying node.

For the unrestrained cases, the pipe length was set to be equal to 20 times the mean diameters.



**Figure I.19 Typical finite element mesh for the asymmetric case by Participant E**

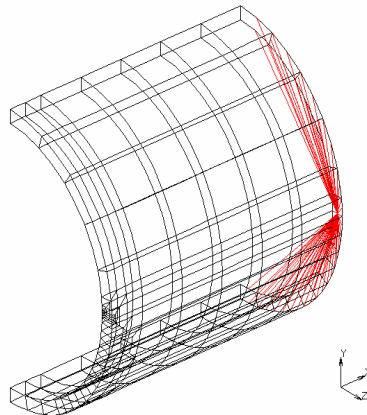


**Figure I.20 Typical finite element mesh used by Participant F**

**Table I.8 Summary of model features**

	<b>Participant A</b>	<b>Participant B</b>	<b>Participant C</b>	<b>Participant D</b>	<b>Participant E</b>	<b>Participant F</b>
<b>Pipe length</b>	Restraint length	$30D_m$ , $50D_m^{(*)}$	Restraint length	$20D_m$ , $30D_m^{(*)}$	Restraint length	Restraint length
<b>Simulation of restraint</b>	At pipe end	On restraint length	At pipe end	On restraint length	At pipe end	At pipe end
<b>Application of axial load</b>	Concentrated force at the TIE node	Uniform stress at restraint plane	Concentrated force at the TIE element	Uniform stress at restraint plane	Uniform displacement at pipe end	Concentrated force at the tying node
<b>Element type</b>	3D 20-node brick	3D 20-node brick	3D 20-node brick with reduced integration	3D 8-node brick with reduced integration	3D 20-node brick	3D 20-node brick
<b>Number of element layer through wall thickness</b>	1	2	1	1	2	1
<b>Mesh refinement</b>	Refined regular mesh at crack tip	Focused mesh at crack tip	Focused mesh at crack tip	Regular mesh	Focused mesh at crack tip	Focused mesh at crack tip
<b>FEM code</b>	ABAQUS	ABAQUS	ABAQUS	ABAQUS	ABAQUS	MARC

<sup>(\*)</sup> for symmetric and asymmetric restraint, respectively.

#### I.2.4 Remarks On Modeling Approaches

Clearly, there are some marked differences among the modeling approaches used by the six participants. Except for Participant D, all other participants used 20-noded second order solid brick elements and the focused mesh around the crack tip. The number of element layers through the pipe wall thickness was divided: four participants used 1 layer of elements whereas the other 2 participants used 2 layers. Moreover, different approaches were employed to deal with the restraint length and the application of the axial load, reflecting the differences in participants' interpretation of the restraint condition in the actual pipe systems. Table I.8 summaries the major features of each participant's modeling approach.

#### I.2.5 Results And Discussion

**I.2.5.1 Effect of Pipe Length on COD of Unrestraint Pipe** - The problem statement did not specify the pipe length for the COD calculation of the unrestrained pipe (i.e., the end-capped vessel). Theoretically, it should be infinitely long. Both Participants C and F investigated the effect of the pipe length on COD of the unrestrained pipe. Figure I.21 shows the results by Participant F for the longest crack length ( $\theta=\pi/2$ ), where  $\theta$  is half the total crack length. Clearly, pipe lengths greater than  $20D_m$ , as used for all the participants, are sufficiently long for the COD calculations for the unrestrained pipe.

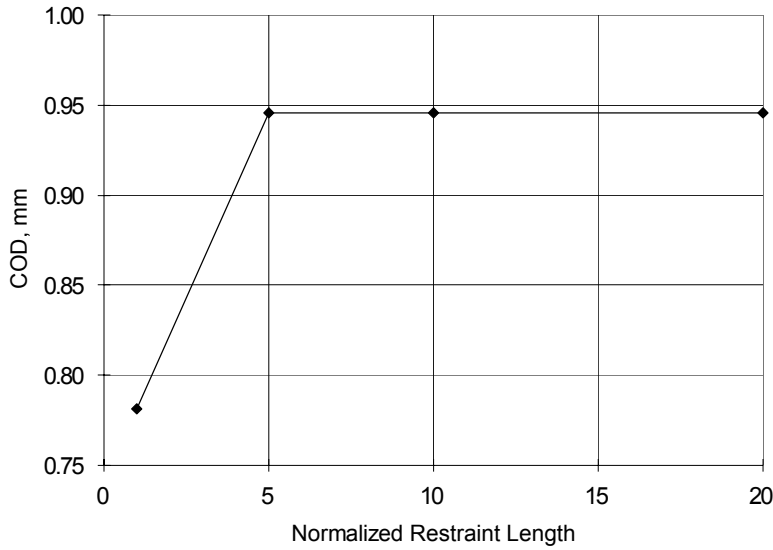


**Figure I.21 Effect of pipe length on COD of unrestrained pipe for the longest crack length investigated in this program. Participant F**

**I.2.6 Comparison of Round-Robin (Case 1) Results**

**I.2.6.1 Comparison of COD Values in Unrestrained Pipes - Error! Reference source not found.** I.22 shows the comparison of the COD values of the unrestrained pipes (the end-capped vessel case) obtained by all participants

for the common round-robin cases ( $R_m/t = 10$ ). The COD values are normalized by the mean COD value of all participants for the same case. Overall, the results from Participant C, E, and F are consistent among each other. The discrepancies are within 1% from the mean COD value averaged among these three participants, as shown in Figure I.23.

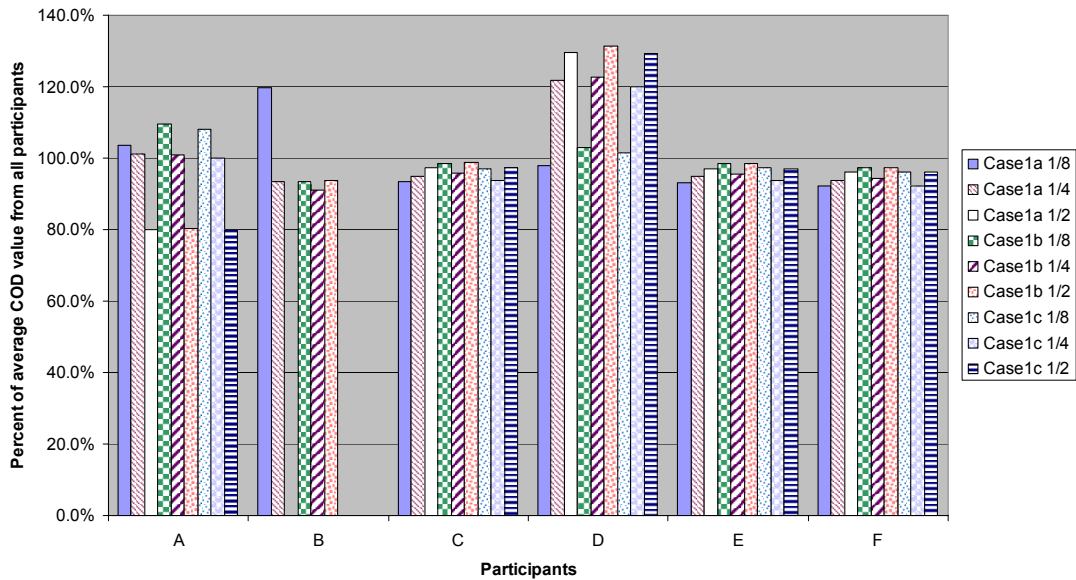


**Figure I.22 Comparison of the unrestrained COD values for Cases 1a-1c. The COD values are normalized with respect to the averaged COD value of all participants**

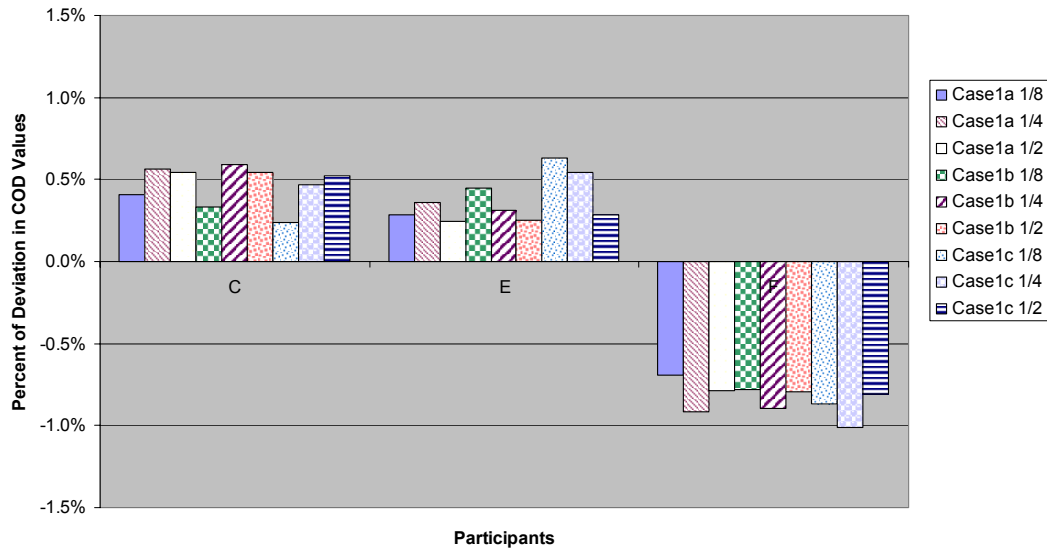


**Figure I.23 Comparison of the unrestrained COD values from Participant C, E, and F for Cases 1a-1c. The COD values are normalized by the mean COD value of the three participants of the same case**

For the two shorter crack lengths ( $\theta=\pi/8$ , and  $\theta=\pi/4$ ), the COD values from Participant A were close to the average. However, the CODs of the longest crack length ( $\theta=\pi/2$ ) were only 80% of the averaged values.

Participant B also did reasonably well, except for one particular case (Case 1a,  $\theta=\pi/8$ ) where the COD was about 120% of the mean value.

The biggest discrepancies were from Participant D for the two long crack cases ( $\theta=\pi/4$  and  $\theta=\pi/2$ ). The COD values are over 20 percent higher than the mean values. Table I.9 summarizes the observations on the unrestrained COD comparisons.

**Table I.9 Observations on unrestrained pipe case**

Participant	Comparison to average from group	Case by case scatter
A	Lower for longest crack length	Significant
B	About the same	One case much higher
C	Very close	Very low
D	Much higher	Significant
E	Very close	Very low
F	Very close	Very low

**I.2.6.2 Effect of Pipe Diameter** - Despite the fact that the COD values for a specific case

could be different, among the different participants all participants reported that the pipe

diameter has no noticeable effect on the *normalized* COD values for all the cases in Case 1. The normalized COD only depends on the crack length,  $R_m/t$  ratio, and the restraint length. This is illustrated from the data of Participants A

and C in Figures I.24 and I.25, respectively. The independence of COD on pipe diameter simplifies the comparison of the round-robin results (Case 1) – it is unnecessary to distinguish the results from different diameter pipes.

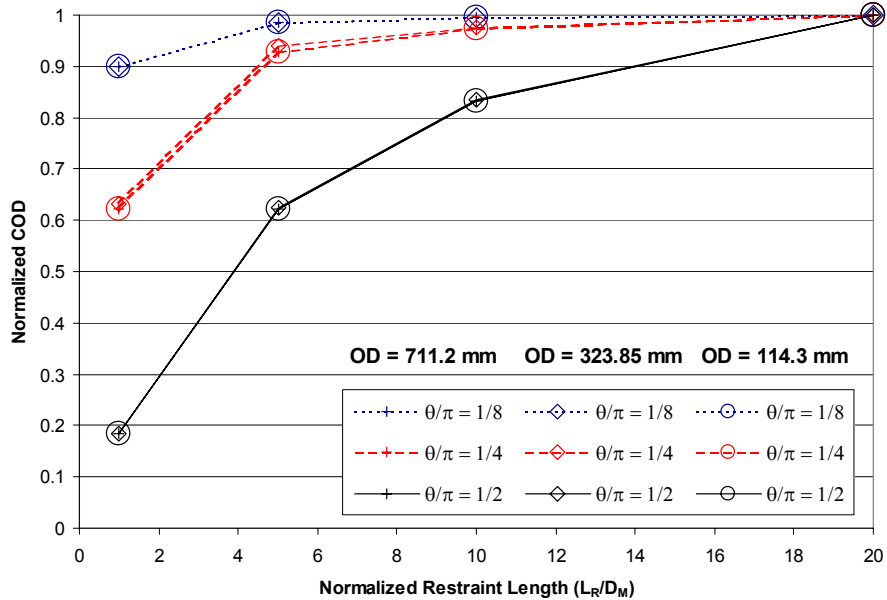


Figure I.24 Normalized COD values for Case 1a-1c from Participant A

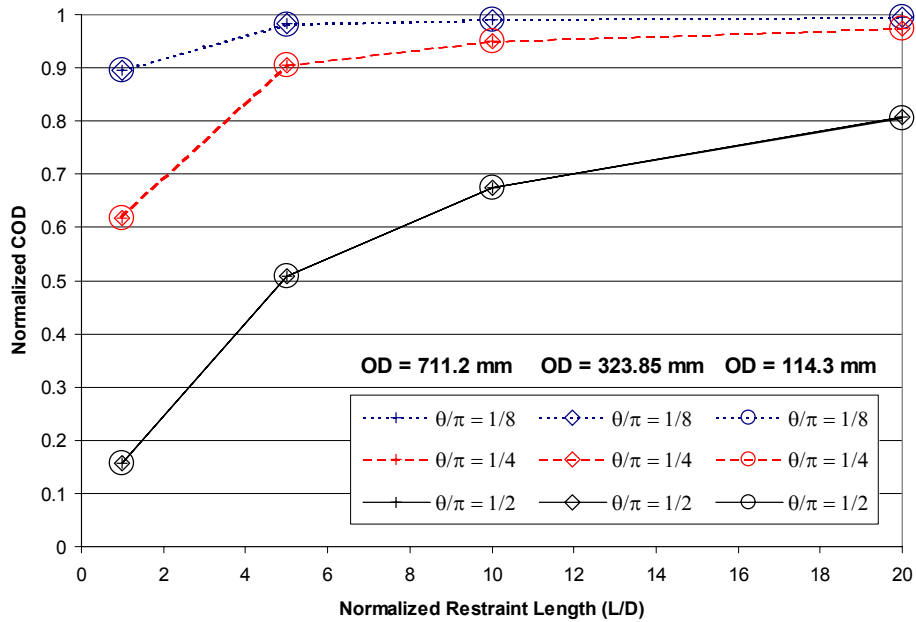


Figure I.25 Normalized COD values for Case 1a-1c from Participant C

**I.2.6.3 Comparison of Restraint Cases in Case 1** – Figure I.26 through Figure I.28 show the normalized COD, respectively for each of the crack lengths investigated in the common round-robin cases. Also shown in these figures are the results reported in NUREG/CR-6443 (Ref. I.1). Overall, all participants reported the same trends on the effects of the restraint length and crack length on the normalized COD. The results from Participant C and F are always consistent for all the cases in the round-robin.

The normalized COD calculated by Participant D were consistently lower than those by the other five participants. This might be attributed to the use of the one-layer, first-order elements and the non-focused mesh around the crack tip by Participant D. Also troublesome was the use of uniformed stress to apply the axial load by

Participant D. The previous results reported in NUREG/CR-6443 (Ref. I.1) also show noticeable discrepancies when compared with the round-robin results.

Excluding the results from Participant D, the results from all other five round-robin participants are plotted in Figure I.29, for all the round-robin cases. The results are quite consistent for the two short lengths ( $\theta=\pi/8$ , and  $\theta=\pi/4$ ), with the exception of one data point from Participant B at ( $L/D=1$  and  $\theta=\pi/4$ ). On the other hand, there is noticeable scatter for the cases with the longest crack length ( $\theta=\pi/2$ ).

Table I.10 summarizes the comparison of the round-robin cases among all participants.

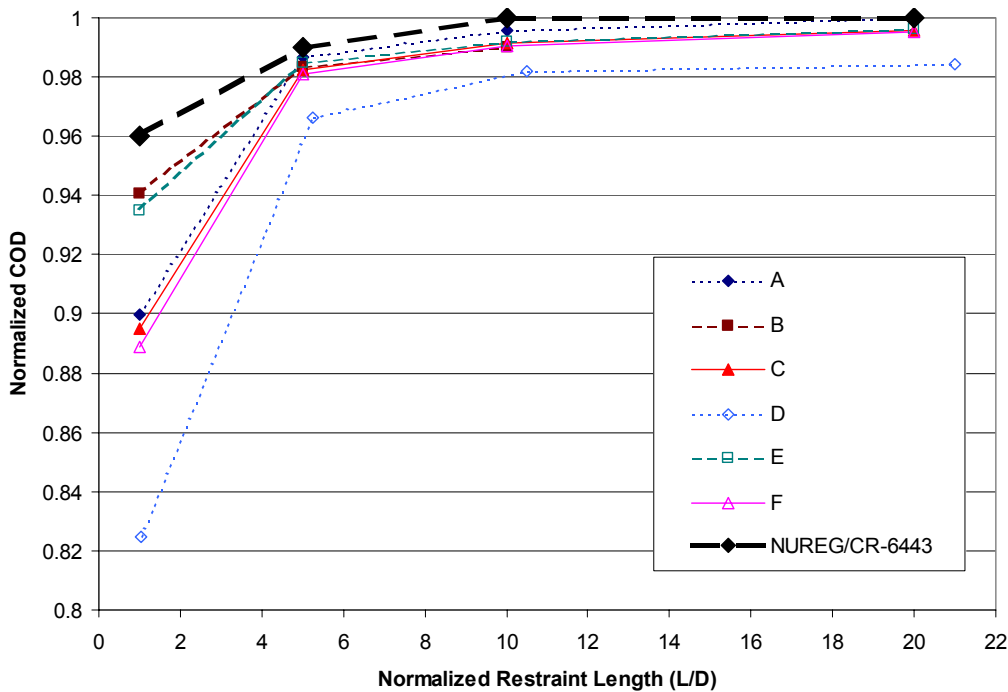


**Figure I.26 Comparison of normalized COD in Case 1, half crack length =  $\pi/8$**

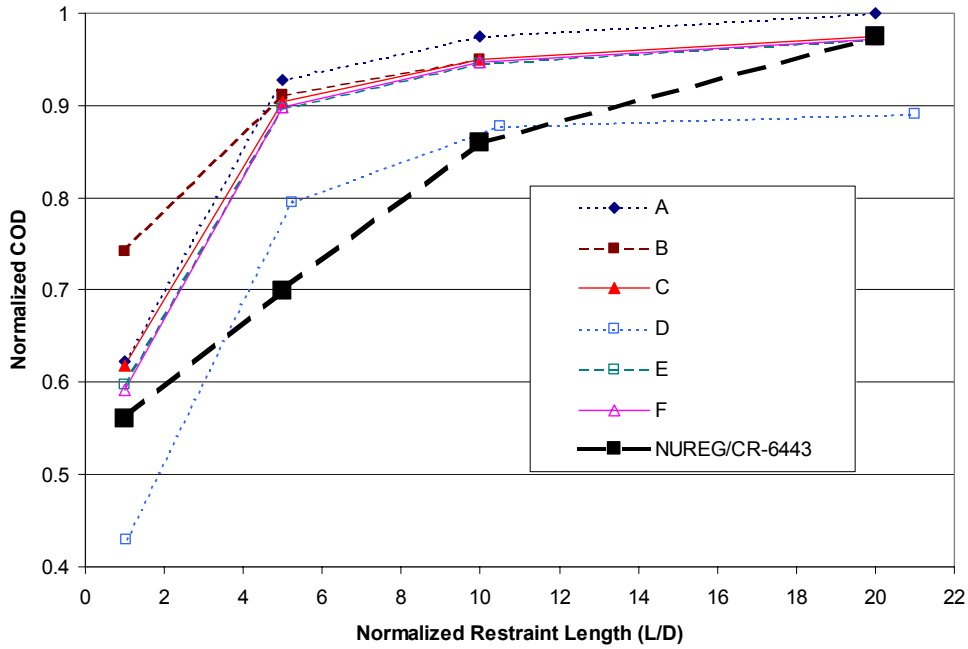


Figure I.27 Comparison of normalized COD in Case 1, half crack length =  $\pi/4$

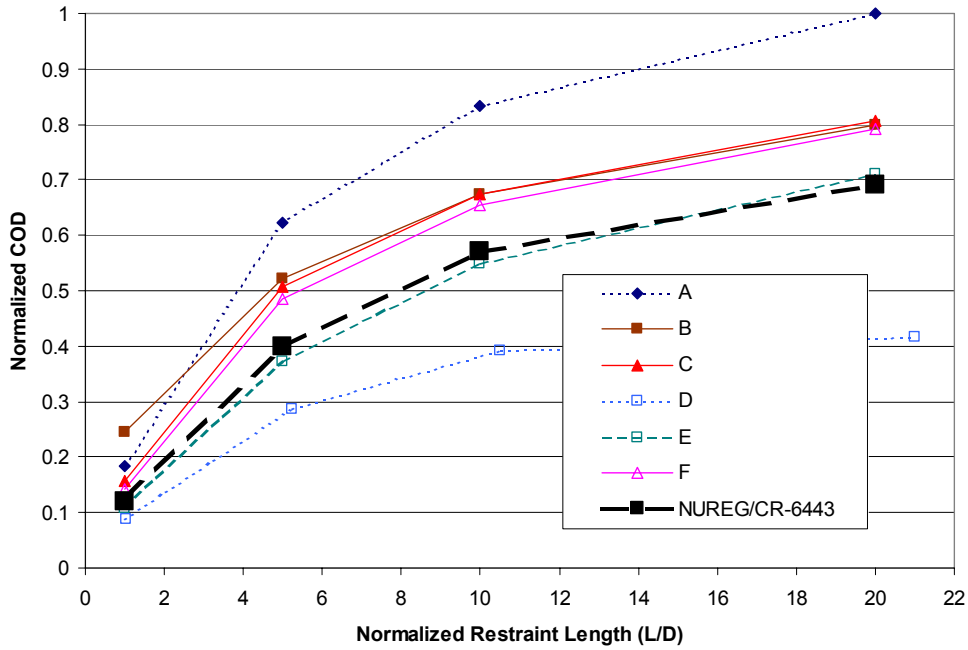
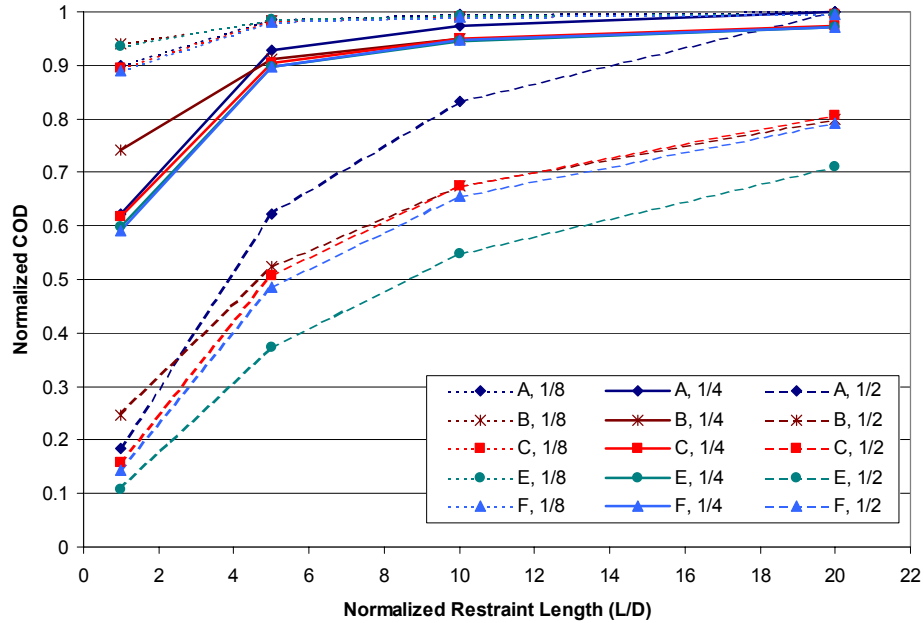


Figure I.28 Comparison of normalized COD in Case 1, half crack length =  $\pi/2$



**Figure I.29 Comparison of normalized COD for all round-robin cases in Case 1, excluding the results from Participant D and NUREG/CR-6443 (Ref. I.1)**

**Table I.10 Observations on the round-robin case comparisons**

Participant	Comparison to Average from Group
A	Agrees with C, F for $\theta=\pi/8$ and $\pi/4$ but higher for $\theta=\pi/2$
B	Agrees with C, F except for shortest restraint length
C, F	Agree with each other all the time and in the middle of entire group results
D	Generally lower than others
E	Agrees with C, F for $\theta=\pi/8$ and $\pi/4$ but lower for $\theta=\pi/2$
NUREG/CR-6443	Highest for short flaws, lower than C, F for longer flaws

**I.2.7 Effect of  $R_m/t$  Ratio (Case 2)**

The effects of  $R_m/t$  ratio on the normalized COD are analyzed by comparing the results in Case 1 and Case 2. As shown in Table I.4, only four

participants took part in Case 2, and each participant analyzed a subset of Case 2. The results are presented in Figure I.30 through Figure I.33. The normalized COD increases as  $R_m/t$  ratio decreases.

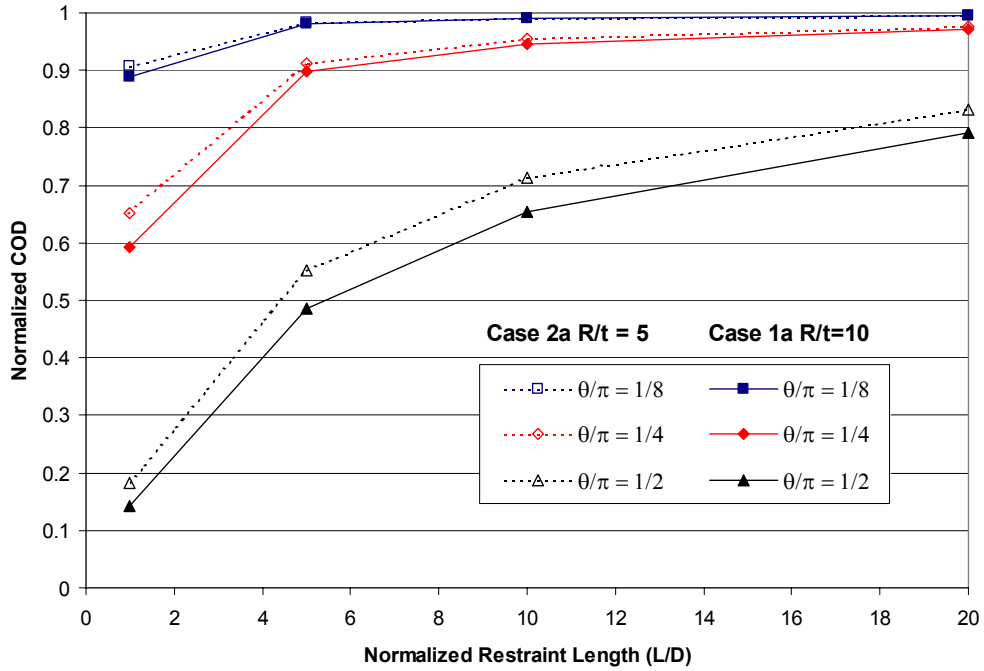


Figure I.30 Effect of  $R_m/t$  ratio on normalized COD. Participant F, OD=28-inch

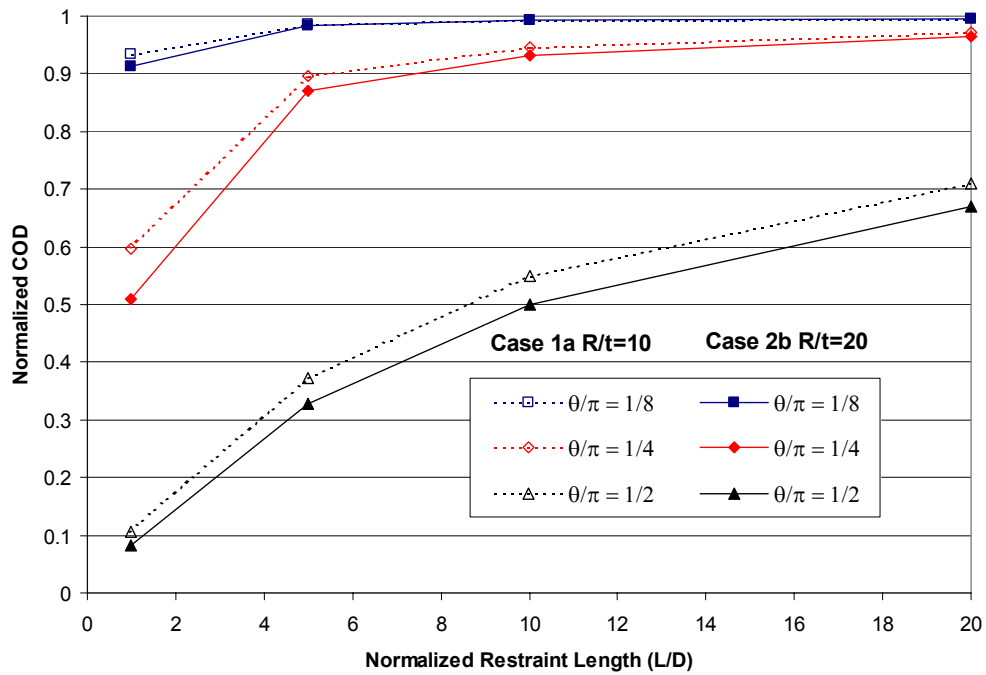


Figure I.31 Effect of  $R_m/t$  ratio on normalized COD. Participant E, OD=28-inch

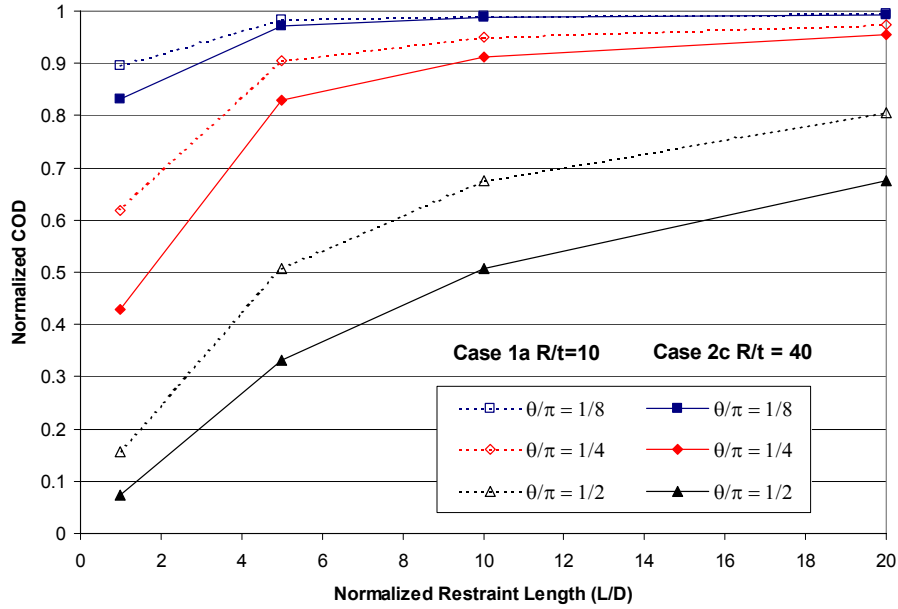


Figure I.32 Effect of  $R_m/t$  ratio on normalized COD. Participant C, OD=28-inch

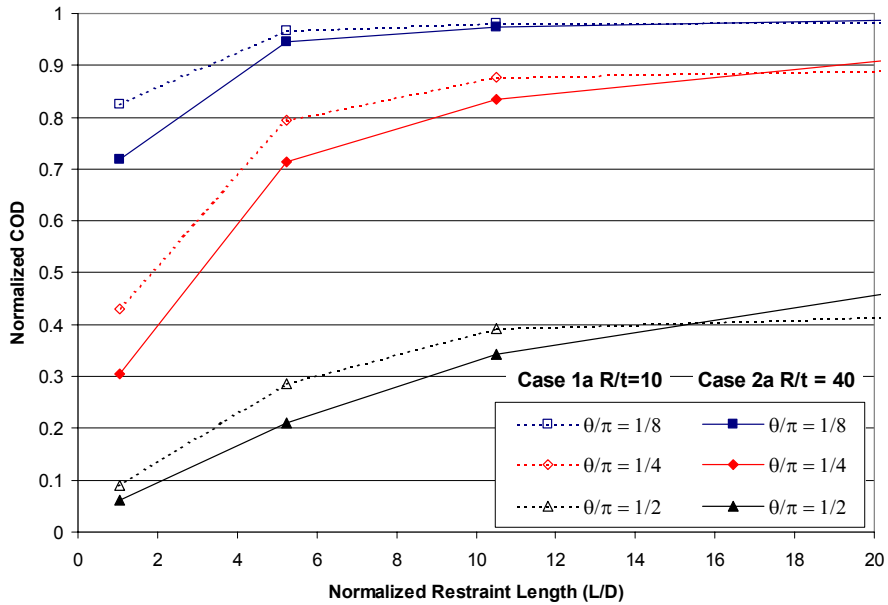


Figure I.33 Effect of  $R_m/t$  ratio on normalized COD. Participant D, OD=28-inch

### I.2.8 Effect of Asymmetric Restraint Length (Case 3)

Similar to Case 2, each participant was assigned to solve a subset of Case 3. The results are tabulated in Table I.11 to Table I.13. The effects of non-symmetric restraint are depicted in Figure I.34 to Figure I.36, using a subset of the

results. Similar to the effect of reducing the symmetric restraint length from both sides of the crack plane, the normalized COD value decreases as the restraint length from one side of the crack plane is shortened. The effect of the asymmetric restraint length is more pronounced as the asymmetry in the restraint length increases. However, significant reductions from

the normalized COD of the symmetrically restrained pipe only exist when the crack length

is longest ( $\theta=\pi/2$ ), or the restraint length on one side of the crack plane is very short ( $L_2/D = 1$ ).

**Table I.11 Normalized COD under asymmetric restraint length, OD=28-inch**

Case 3a Participant F					
$\theta/\pi = 1/8$		L <sub>1</sub> /D			
		1	5	10	20
L <sub>2</sub> /D	1	0.888915	0.924125	0.93891	0.95639
	5		0.981084	0.983291	0.984323
	10			0.990476	0.991539
	20				0.995292
$\theta/\pi = 1/4$		L <sub>1</sub> /D			
		1	5	10	20
L <sub>2</sub> /D	1	0.59183	0.68585	0.736959	0.805576
	5		0.897811	0.908835	0.914071
	10			0.94623	0.952008
	20				0.972409
$\theta/\pi = 1/2$		L <sub>1</sub> /D			
		1	5	10	20
L <sub>2</sub> /D	1	0.143176	0.203258	0.251817	0.349994
	5		0.484868	0.516988	0.533301
	10			0.655057	0.681819
	20				0.792594

**Table I.12 Normalized COD under asymmetric restraint length, OD=12.75-inch**

Case 3b Participant B					Case 3b Participant E						
$\theta/\pi = 1/8$		L <sub>1</sub> /D				$\theta/\pi = 1/8$		L <sub>1</sub> /D			
		1	5	10	20			1	5	10	20
L <sub>2</sub> /D	1	0.940865	0.950959	0.958131	0.969925	L <sub>2</sub> /D	1	0.935	0.963	0.974	0.979
	5		0.983497	0.977444	0.985965		5		0.986	0.991	0.995
	10			0.991099	0.99199		10			0.993	0.996
	20				0.995303		20				0.997
$\theta/\pi = 1/4$		L <sub>1</sub> /D				$\theta/\pi = 1/4$		L <sub>1</sub> /D			
		1	5	10	20			1	5	10	20
L <sub>2</sub> /D	1	0.742396	0.774126	0.803464	0.853369	L <sub>2</sub> /D	1	0.597	0.8	0.86	0.899
	5		0.910451	0.919498	0.922728		5		0.896	0.928	0.955
	10			0.950063	0.954941		10			0.945	0.964
	20				0.973478		20				0.972
$\theta/\pi = 1/2$		L <sub>1</sub> /D				$\theta/\pi = 1/2$		L <sub>1</sub> /D			
		1	5	10	20			1	5	10	20
L <sub>2</sub> /D	1	0.245671	0.275446	0.313982	0.40025	L <sub>2</sub> /D	1	0.113	0.273	0.404	0.549
	5		0.522858	0.54151	0.550999		5		0.399	0.502	0.628
	10			0.673468	0.697404		10			0.574	0.669
	20				0.798483		20				0.73

**Table I.13 Normalized COD under asymmetric restraint length, OD=4.5-inch**

Case 3c Participant C					Case 3c Participant D						
$\theta/\pi = 1/8$		L <sub>1</sub> /D				$\theta/\pi = 1/8$		L <sub>1</sub> /D			
		1	5	10	20			1	5	10	20
L <sub>2</sub> /D	1	0.895167	0.929368	0.944238	0.959108	L <sub>2</sub> /D	1	0.824699	0.869431	0.889782	0.916129
	5		0.982156	0.98513	0.98513		5		0.966211	0.980468	0.983354
	10			0.991078	0.992565		10			0.98193	0.994099
	20				0.995539		20				0.984239
$\theta/\pi = 1/4$		L <sub>1</sub> /D				$\theta/\pi = 1/4$		L <sub>1</sub> /D			
		1	5	10	20			1	5	10	20
L <sub>2</sub> /D	1	0.617438	0.705071	0.756228	0.824066	L <sub>2</sub> /D	1	0.429606	0.49354	0.542892	0.628249
	5		0.904359	0.914146	0.919706		5		0.79474	0.826453	0.841462
	10			0.949956	0.955294		10			0.877329	0.900642
	20				0.974199		20				0.890479
$\theta/\pi = 1/2$		L <sub>1</sub> /D				$\theta/\pi = 1/2$		L <sub>1</sub> /D			
		1	5	10	20			1	5	10	20
L <sub>2</sub> /D	1	0.157449	0.218215	0.270808	0.373945	L <sub>2</sub> /D	1	0.089451	0.12277	0.137155	0.207064
	5		0.507238	0.539204	0.555338		5		0.286485	0.315024	0.337098
	10			0.67491	0.700694		10			0.391355	0.453497
	20				0.806393		20				0.416638

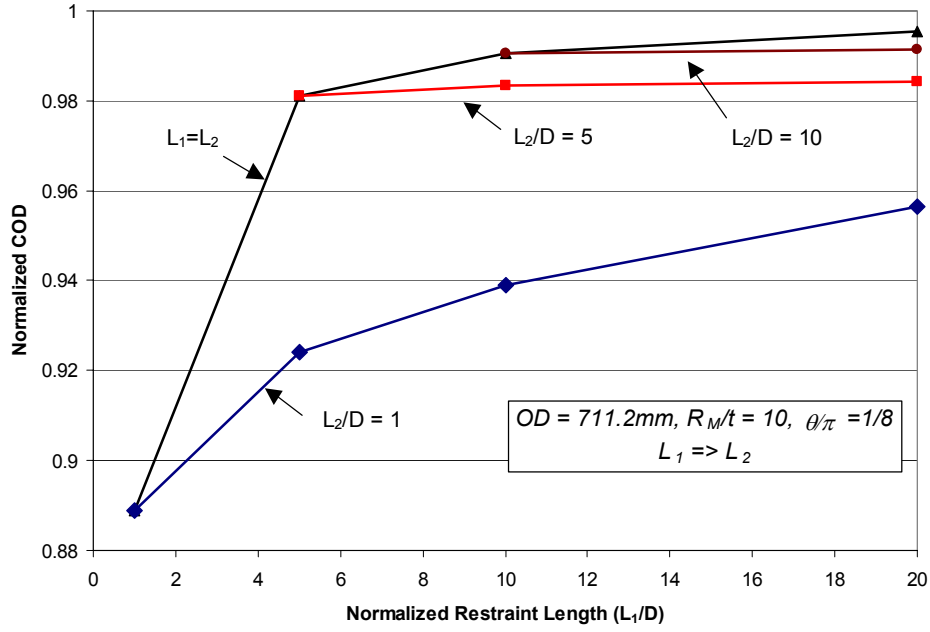


Figure I.34 Normalized COD under asymmetric restraint length from Participant F

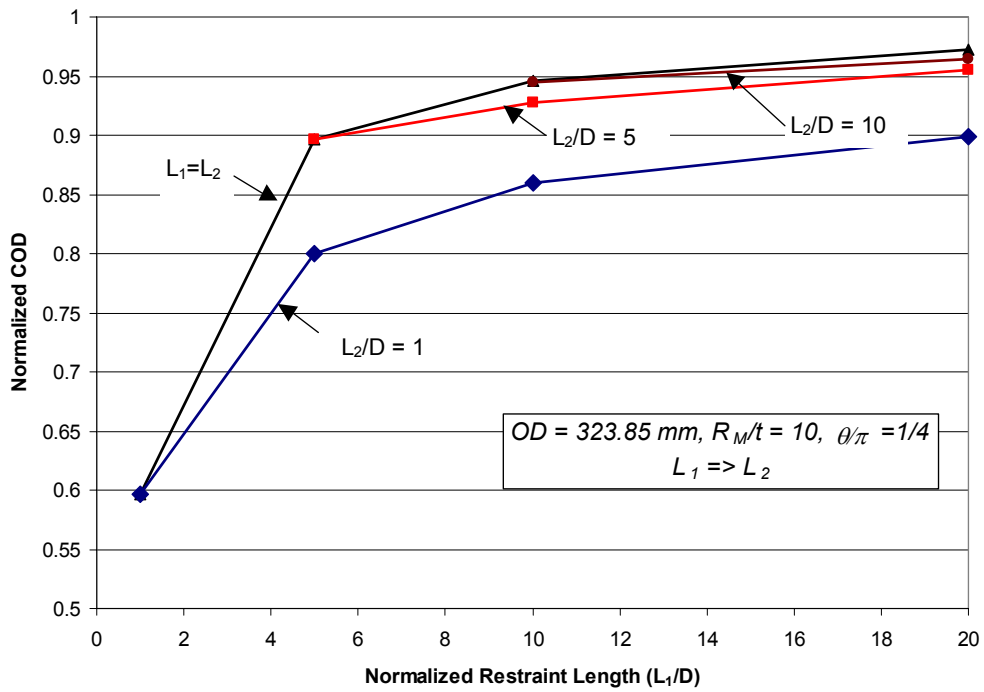


Figure I.35 Normalized COD under asymmetric restraint length from Participant E

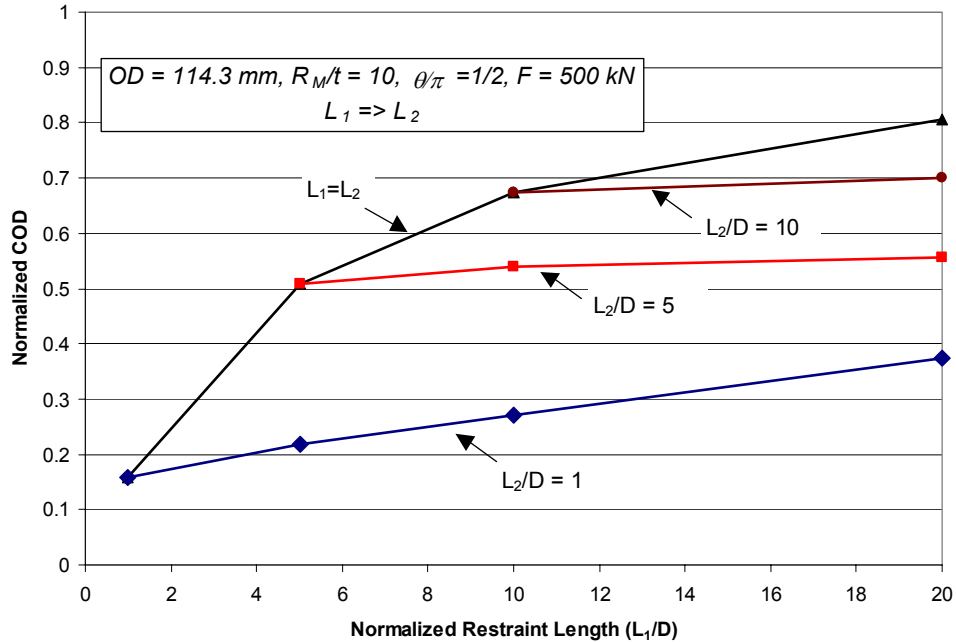


Figure I.36 Normalized COD under asymmetric restraint length from Participant C

### I.2.9 Summary of First Round Robin Analyses

Six organizations from three countries participated in this first round robin analysis to investigate the effect of pipe-system restraint on the linear elastic COD values in axially loaded pipe systems. The results from the round-robin cases revealed that:

- The results from Participant C and F agree with each other for all the cases analyzed, and are in the middle of group results.
- The results from Participant A agree with those of Participants C and F, except for the cases of the longest crack length ( $\theta=\pi/2$ ) where the CODs of unrestrained pipe are significantly lower, and the normalized CODs are significantly higher.
- The results from Participant B agree with those of Participants C and F, except for the cases of shortest restraint length ( $L/D=1$ ).
- The results from Participant D show lower normalized CODs for the restrained pipes and higher CODs for the unrestrained pipes, when compared to those of the other participants. These discrepancies might be

attributed to the use of first-order, unfocused elements by Participant D.

- The results from Participant E agree with those of Participants C and F, except that the normalized COD for the longest crack length ( $\theta=\pi/2$ ) are significantly lower.

Other findings from this study include:

- The pipe diameter has negligible effect on the normalized COD results.
- As the  $R_m/t$  ratio increases, the restraint effect increases, resulting in lower normalized COD values.
- As the difference in the restraint lengths from the two sides of the crack increases, the asymmetric restraint effect on the normalized COD increases. The effect becomes significant once one of the restraint lengths is reduced to  $L/D=1$ , or the crack length is longest ( $\theta=\pi/2$ ).

### I.3 SECOND ROUND ROBIN (EFFECT OF R/T RATIO ON SURFACE FLAWED PIPE EPFM ANALYSES)

#### I.3.1 Background

One of the objectives of the ASME Section XI Working Group on Pipe Flaw Evaluation is to extend the flaw evaluation criteria to other than Class 1 piping. The extension of the in-service flaw evaluation criteria to Class 2, 3, and balance-of-plant (BOP) piping has two aspects that require further development than needed for Class 1 piping. The first is that these piping systems may operate at lower pressures, and hence have higher radius-to-thickness ( $R/t$ ) ratios. The second is the lower operating temperature effects on the fracture behavior of ferritic steels. This round-robin problem focused on the  $R/t$  effects on the crack-driving force relationships.

#### I.3.2 Past Round-Robin and FE Efforts

Over the years, there has been many efforts aimed at developing a better solution to the problem of determining an analysis procedure to predict the failure loads of a pipe with a circumferential surface crack under pressure, axial tension, and bending loads. The initial efforts focused on Class 1 pipe that operates at higher temperatures and is generally thicker-walled pipe ( $R/t < 15$ ). In the early developmental efforts, there was concern over the accuracy of finite element (FE) solutions, and the ability to use those results to develop or validate simpler closed-form solutions that could lead to a codified procedure.

One of the initial efforts was a 1986 ASME PVP round-robin (RR) analysis of a surface-cracked pipe test (Ref. I.3). This involved a 16-inch diameter schedule 100 A106B pipe, where the crack was 66-percent of the pipe thickness for the entire length of half of the pipe circumference, see Figure I.37.

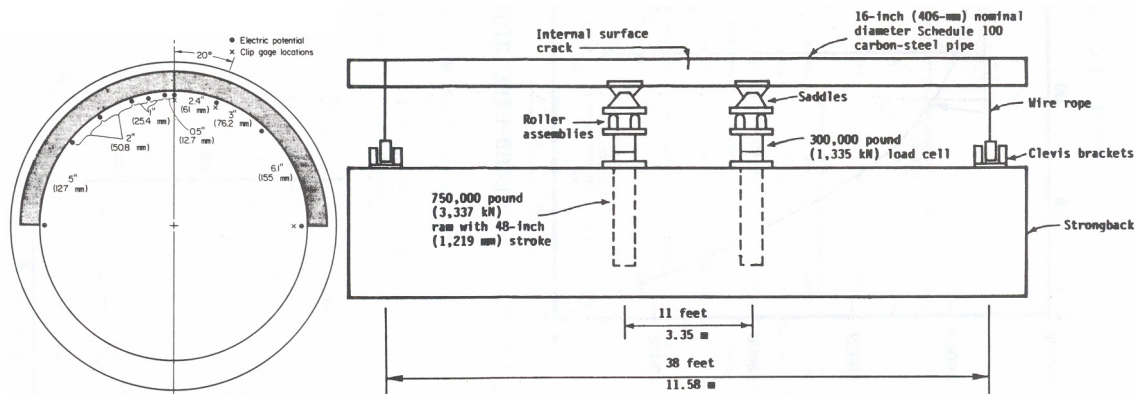
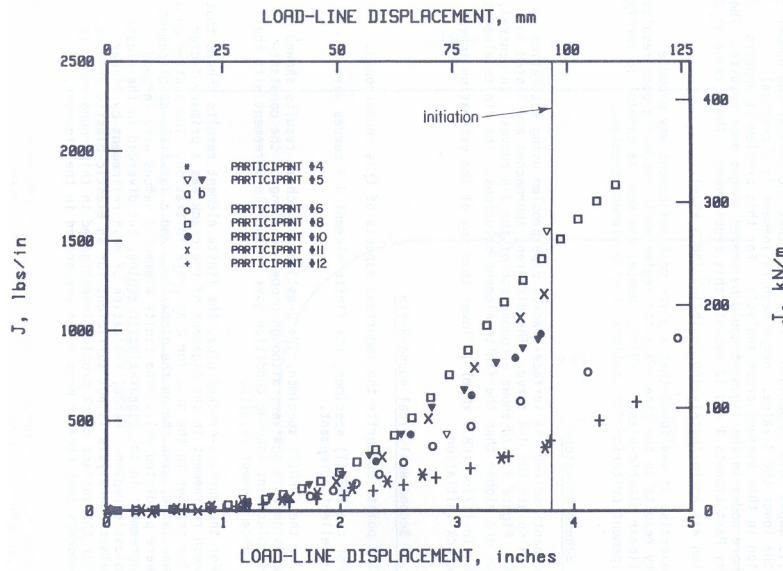


Figure I.37 Pipe test analyzed in 1986 ASME PVP round robin

The  $J$  versus load-line displacement values from all the 3D analyses at that time are given in 38. There was considerable scatter in the plastic region, and the mesh refinement in the ligament was found to be the major concern, see Figure I.39. Figure I.40 shows the results from that

same round robin when the participants used different estimation schemes. The 1986 results showed that FE meshing was important, and that there was considerable scatter in the estimation scheme results.



**Figure I.38 Results for 3D FE analysis of 1986 ASME PVP round robin -  $J$  versus load-line displacement**

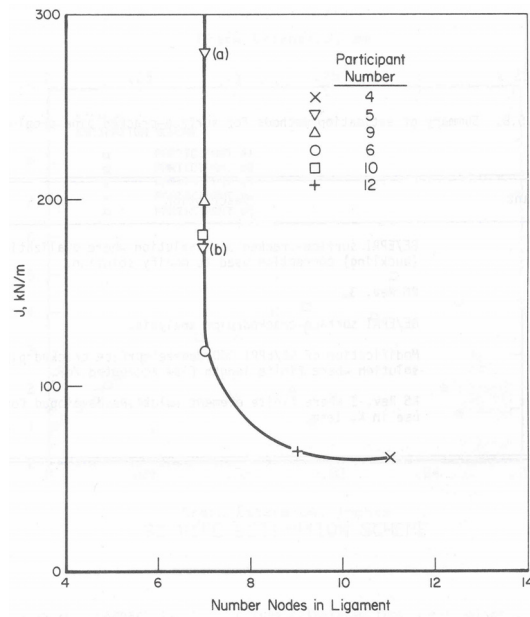


**Figure I.39 Results for 3D FE analysis of 1986 ASME PVP round robin -  $J$  values at initiation displacement versus number of nodes in ligament of FE model**

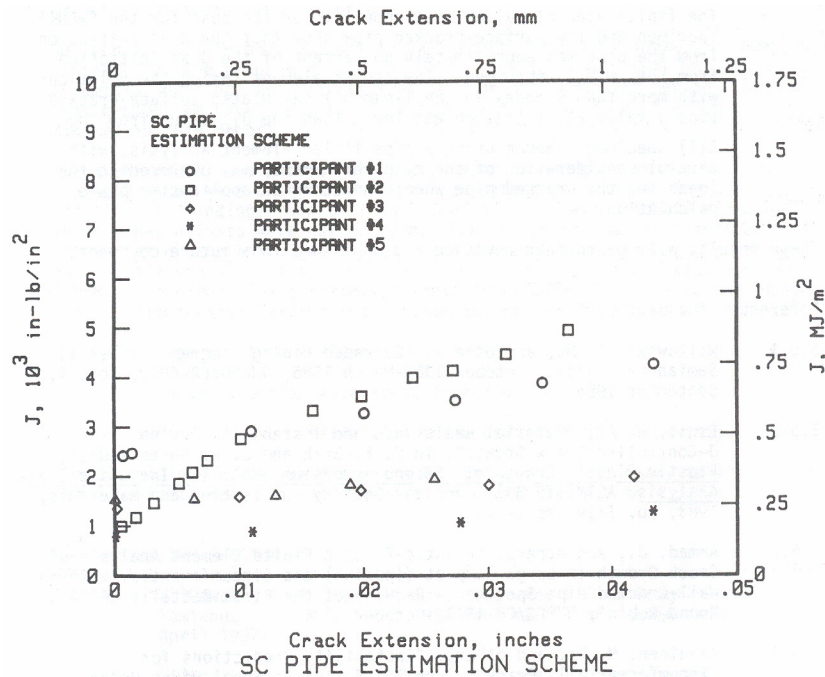


**Figure I.40 Results for estimation analysis of 1986 ASME PVP round robin**

The work in the 1986 round robin also spurred additional analyses afterwards. For instance, Brickstad conducted analyses using line-spring elements in ABAQUS as part of the Swiss/Swedish Cooperative Program that was presented at 7th IPIRG-1 TAG meeting in November, 1989 (Ref. I.4), Shimakawa and Yagawa (Ref. I.5), Doi et al. (Ref. I.6), Takahashi et al. (Ref. I.7), and Miyoshi (Ref.

I.8) also did 3D analyses of the 1986 PVP RR with more refined meshes. Miyoshi had the finest mesh. The results of the  $J$  values at the displacement that corresponded to experimentally measured crack initiation are given in Table I.14. Figure I.41 shows that the Brickstad line-spring results compared very closely to the Miyoshi 3D analysis with the finest mesh.

**Table I.14 Post round-robin analyses of the 1986 ASME round-robin problem**

	$J$ at initiation, $\text{MJ/m}^2$
Brickstad (Line-spring)	0.235
Shimakawa and Yagawa, (3D)	0.213
Doi et al., (3D)	0.194
Takahashi et al., (3D)	0.185
Miyoshi (3D – finest mesh)	0.264

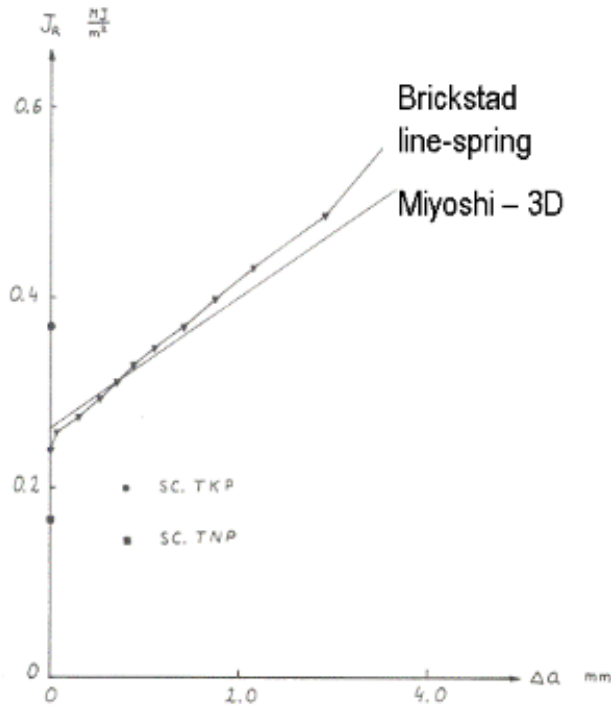


**Figure I.41 Comparison of Brickstad and Miyoshi results showing good agreement between line-spring and very refined 3D FE results**

Another round-robin effort for circumferential surface cracks was conducted in the IPIRG-1 program, i.e., Round-Robin Problem 2-1. The results of that round robin are summarized in NUREG/CR-6233 Vol. 4 (pg 2-107) (Ref. I.9). This IPIRG-1 round-robin problem involved estimation scheme analyses of an aged cast stainless steel pipe test under pressure and quasi-static bending, i.e., 16-inch diameter, Schedule 100,  $R/t = 8$ , pressure of 15.5 Mpa (2,250 psi), and test temperature of 288C (550F). Predictions were made of crack initiation and maximum load given an actual tensile stress-strain curve and L-C C(T) specimen  $J$ - $R$  curves. Table I.15 presents a summary of the initiation load predictions, and the maximum load predictions are given in Table I.16 The difference in the load predictions was much greater than desired, and some participants had significant differences even though they used the same basic analysis procedure.

Another effort that is of value to summarize here is from Mohan, where he compared 3D and line-spring FE results in an IPIRG-2 report for elbow applications (Ref. I.10). Mohan first conducted an analysis to validate the line-spring approach against full 3D FE analyses for straight-pipe with a circumferential surface crack (Ref. I.10). This was done for the same 1986 ASME PVP RR problem, i.e., DP3II Experiment 4112-8. Those results showed that the line-spring analysis gave good agreement with a full 3D brick element analysis when sufficient mesh refinement was used, see Figure I.42. Additionally, Mohan compared full 3D FE results for a surface crack in an elbow to results from using line-spring elements (Ref. I.10). Those results also showed good agreement, see Figure I.43.

**Table I.15 Initiation load predictions from IPIRG-1 round-robin using estimation schemes**

	Load, kN	Moment, kN-m	<u>Predicted</u> <u>Experimental</u>
Experimental	319.1	656.6	
Participant A			
R6-Option 1	179.2	368.5	0.56
R6-Option 2	199.7	410.6	0.63
Participant B			
R6-Option 3	301.8		0.95
Participant C			
J <sub>T</sub> Analysis	173.1		0.54
Participant D			
R6-Case 1	314.7		0.99
R6-Case 2	285.5		0.89
Participant E			
EPFM (with Press. Corr.)			
SC.TNP 1		634.1	0.97
SC.TKP 1		465.7	0.71

**Table I.16 Maximum load predictions from IPIRG-1 round-robin using estimation schemes**

	Load, kN (kip)	Moment, kN-m (in-lb)	<u>Predicted</u> <u>Experimental</u>
Experimental	326.8 (73.4)	672.5 (5.95x10 <sup>6</sup> )	
Participant B	301.8 (67.8)		0.92
Participant C			
IWB-3640	259.6 (58.3)		0.79
J <sub>T</sub> Analysis	245.7 (55.2)		0.75
J <sub>T</sub> Analysis	293.7 (66.0)		0.90
Net-Section-Collapse	366.3 (82.3)		1.12
Participant D			
R6-Case 1	330.5 (74.3)		1.01
R6-Case 2	313.5 (70.4)		0.96
R6-Case 3	323.2 (72.6)		0.99
Participant E			
Net-Section-Collapse			
1.15 σ-Avg	454.3 (102.1)	934.0 (8.27x10 <sup>6</sup> )	1.39
σ-Avg	385.0 (86.5)	792.0 (7.01x10 <sup>6</sup> )	1.18
3 S <sub>m</sub>	341.0 (76.7)	702.0 (6.21x10 <sup>6</sup> )	1.04
IWB-3640 (No Safety Factor)	254.0 (57.0)	522.0 (4.62x10 <sup>6</sup> )	0.78
DPZP (Best fit for SC)			
1.15 σ-Avg	389.0 (83.6)	799.0 (7.08x10 <sup>6</sup> )	1.19
σ-Avg	351.0 (78.9)	721.0 (6.39x10 <sup>6</sup> )	1.08
EPFM (with Press. Corr.)			
SC.TNP1	363.0 (81.4)	745.0 (6.59x10 <sup>6</sup> )	1.11
SC.TKP1	256.0 (57.4)	525.0 (4.65x10 <sup>6</sup> )	0.78

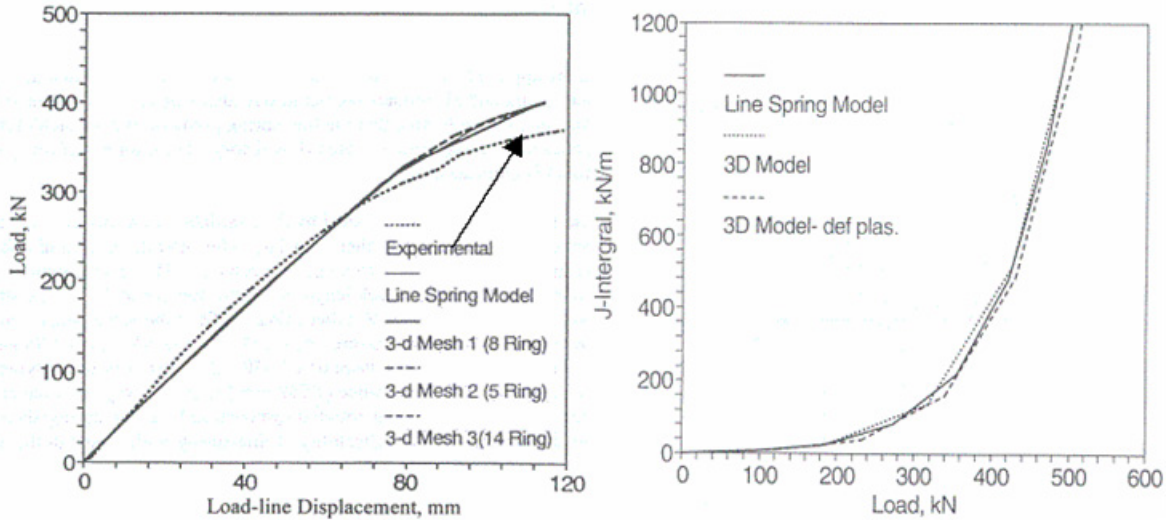


Figure I.42 Comparison of Mohan FE analyses of 1986 ASME PVP round-robin problem

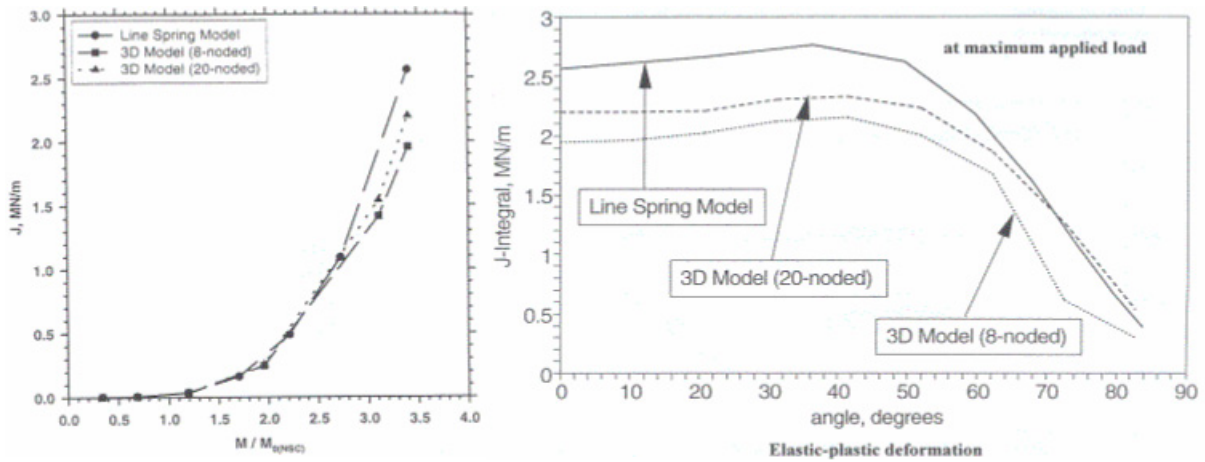


Figure I.43 Comparison of Mohan FE analyses of surface crack in an elbow

### I.3.3 *J*-estimation Scheme Development

The *J*-estimation schemes for surface-flawed pipes have elastic and plastic contributions. The elastic contribution is known from tabulated elastic *F*-functions for global bending and axial tension in the open literature.

The elastic-plastic contributions to *J* are more difficult to establish. During past NRC programs on piping, several circumferential surface-cracked-pipe *J*-estimation schemes were developed for Class 1 piping where the *R/t* ratios were less than 15. These estimation schemes are available in the computer code NRCPIPES (Ref.

I.11). The available options in NRCPIPES are:

- SC.TNP1 and SC.TNP2,
- SC.TKP1 and SC.TKP2, and
- SC.ENG1 and SC.ENG2.

The differences in these solutions are briefly noted below.

SC.TNP1 is the original SC.TNP solution by Ahmad in NUREG/CR-4872 (Ref. I.12). This analysis used the 360-degree GE/EPRI surface-crack *h*-functions with a *thin*-shell assumption in creating circumferential finite length flaw *h*-functions for pipes in bending.

- SC.TNP2 is a modification by Mohan in NUREG/CR-6298 (Ref. I.13). This was a modification to the Ahmad solution where the distance from the crack plane to the point where the unflawed pipe stress distribution existed was calibrated against numerous finite element (FE) analysis results. The original assumption in the Ahmad SC.TNP solution was that this distance was equal to the pipe thickness. Mohan found that this distance ( $L$ ) was equal to the pipe thickness ( $t$ ) times a function of the material strain-hardening exponent ( $n$ ), i.e.,  $L=(n-1)t$ . This relation was derived from pipes with only one  $R/t$  ratio of approximately 7.5.
- SC.TKP1 is the original SC.TKP solution by Ahmad in NUREG/CR-4872 (Ref. I.12). This analysis used the 360-degree GE/EPRI surface-crack  $h$ -functions with a **thick**-shell assumption in creating circumferential finite length flaw  $h$ -functions for pipes in bending.
- SC.TKP2 is a modification by Mohan in NUREG/CR-6298 (Ref. I.13). This was a modification to the Ahmad solution where the distance from the crack plane to the point where the unflawed pipe stress distribution existed was calibrated against numerous finite element analysis results. The original assumption in the Ahmad SC.TKP solution was that this distance was equal to the pipe thickness. Mohan found that this distance ( $L$ ) was equal to the pipe thickness ( $t$ ) times a function of the material strain-hardening exponent, i.e.,  $L=[(n+1)/(2n+1)]t$ . This relation was derived from pipes with only one  $R/t$  ratio of approximately 7.5.
- SC.ENG1 is an estimation scheme developed by Rahman for circumferential surface flaws that parallels the circumferential through-wall-cracked pipe estimation scheme of Brust in NUREG/CR-4853 and NUREG/CR-6235 (Refs. I.14 and I.15). The Brust circumferential through-wall-cracked pipe estimation scheme was called LBB.ENG. Rahman's SC.ENG1 analysis used the **original** net-section-collapse limit-load equations in calculating a parameter  $H(a/t)$ , which was equal to the thickness of the unflawed pipe, divided by an equivalent thickness to reach limit-load conditions.
- SC.ENG2 is an estimation scheme developed by Rahman for circumferential surface flaws that also parallels the through-wall-cracked pipe estimation scheme of Brust (Refs. I.14 and I.15). Rahman's SC.ENG2 analysis used the **Kurihara modification of the original** net-section-collapse limit-load equations in calculating a parameter  $H(a/t)$ , which was equal to the thickness of the unflawed pipe, divided by an equivalent thickness to reach limit-load conditions. The Kurihara solution modified the net-section collapse equations empirically so that they would work better for short deep flaws (Ref. I.16).

In addition to the results shown above, there is another set of interesting calculations. This was work done by Mohan and others for validation of the ASME FAD curve approach in Code Case N494-2 (Ref. I.17). From the work in that paper, it was shown that several investigators got the same moment versus  $J$  values by 3D calculations and line-spring analyses. The results then showed that the Code-Case N494-2 needed a maximum limit of  $R/t$  of 15 to avoid under predicting the crack-driving force, see Figure I.44. Mohan also explored the effect of constant depth versus elliptical flaw shapes on the elastic  $F$ -function.

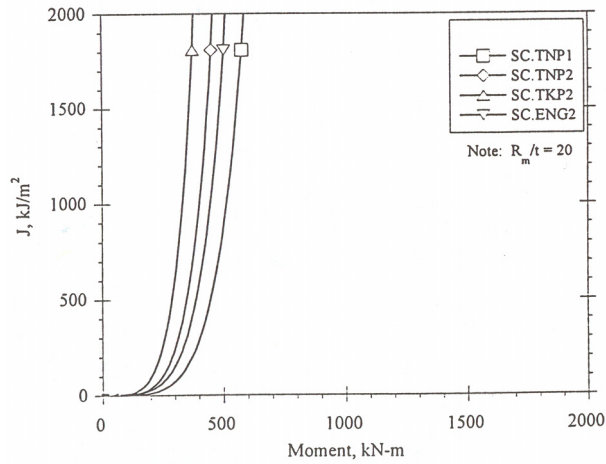
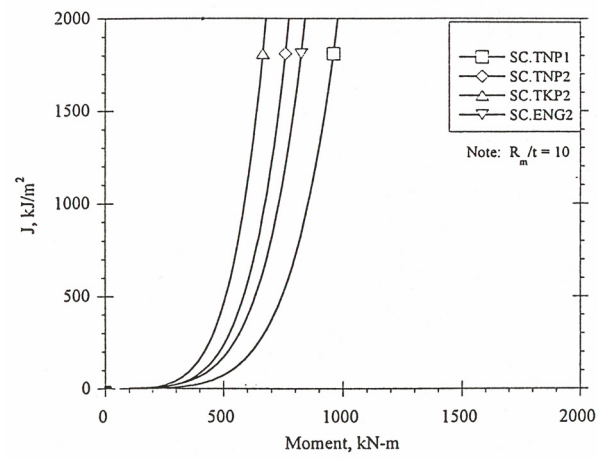
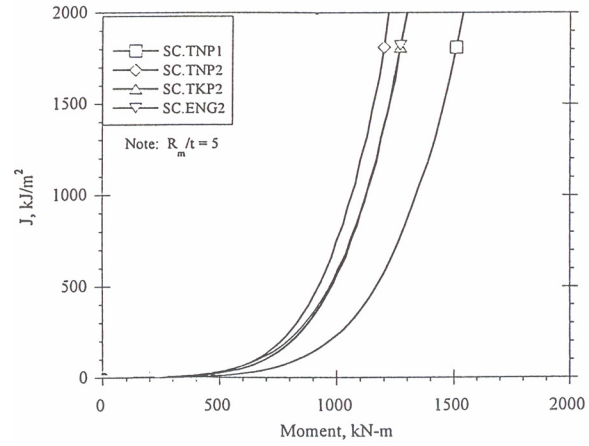


**Figure I.44 Differences in  $J$ -estimation scheme predictions for same diameter pipe with crack dimensions of  $\theta/\pi = 0.5$  and  $a/t = 0.5$  and  $n = 5$**

### I.3.4 Objective of this Round Robin

The objective of this round robin was to evaluate analysis procedures that were capable of providing consistent crack-driving force for higher  $R/t$  pipe. The crack driving force solutions were used to

- assess if any of the estimation schemes in NRCPIPES can be used for higher  $R/t$  pipes, and
- provide procedural basis for the development of  $J$ -estimation schemes for higher  $R/t$  pipe in Class 2, 3, and balance-of-plant piping with internal circumferential surface flaws. The actual development of the schemes is being done as part of a separate BINP task.

### I.3.5 Problem Statement

There were several parts to this round-robin problem. The Problem Set A contained problems for all participants. The results were to be used to check the computation capabilities of all the participants. The Problem Sets B and C involved cases that would expand the numerical solution database for assessing the  $J$ -estimation schemes. The five participating organizations are identified as P1, P2, P3, P4, and P5 in this report. P1 and P3 were in Group 1, and the rest in Group 2.

The participating organizations were tasked to generate  $J$  versus bending moment curves for pipes with internal circumferential surface flaws with or without internal pressure. The surface

flaws were centered in the plane of the bending on the tension side of the pipes. The  $J$  values were taken at the mid-length of the surface cracks, i.e., the location with maximum nominal tension stress. Any analysis approaches deemed appropriate by the individual organization were acceptable. The manner in which the bending moment/displacement was applied was up to the individual participating organization. The end effects from the application of the bending moment/displacement should be minimized.

The stress-strain relation was assumed to obey the generic Ramberg-Osgood power-law hardening relationship,

$$\frac{\varepsilon}{\varepsilon_0} = \frac{\sigma}{\sigma_0} + \alpha \left( \frac{\sigma}{\sigma_0} \right)^n \quad (\text{I.1})$$

where  $\sigma_0$  and  $\varepsilon_0 \equiv \sigma_0/E$  are the reference yield stress and strain, respectively,  $\alpha$  is a dimensionless parameter,  $E$  is the elastic modulus, and  $n$  is the strain hardening exponent.

Three sets of problems and associated participating groups are summarized in Table I.17. The overall dimensions of the pipe is determined by its outside diameter (OD) and the pipe wall thickness ( $t$ ). The size of the flaws is defined by its length ( $\theta$ ), and depth ( $a$ ). The flat-bottom flaws have a constant depth for the entire length. The flaw shape of semi-elliptical cracks corresponds to semi-elliptical flaws in a flat plate that is then transformed into the pipe curvature. The material parameters that define the Ramberg-Osgood stress-strain relationships and the magnitude of applied internal pressure are given in Table I.17.

**Table I.17 Summary of the problem sets and dimensional and material parameters**

Case No.	OD	$t$	$\theta/\pi$	$a/t$	Defect Shape	Elastic Modulus	Poisson's Ratio	$\sigma_0$	$n$	$\alpha$	Internal Pressure	Comments	Participants
	(mm)	(mm)				(GPa)		(MPa)			(MPa)		
A-1	406.4	36.945	0.25	0.500	Flat bottom	182.72	0.30	150.0	5.00	1.00	0.00	Baseline case	Group 1 and Group 2
A-2	406.4	36.945	0.25	0.500	Semi-elliptical	182.72	0.30	150.0	5.00	1.00	0.00	defect shape diff. from A-1	
A-3	406.7	9.500	0.25	0.476	Flat bottom	182.72	0.30	224.0	4.95	5.01	1.55	Pipe experiment 1.2.1.20	Group 1
B-1	406.4	9.912	0.25	0.500	Flat bottom	182.72	0.30	150.0	5.00	1.00	0.00	Based on A-1, $R_m/t=20$	Group 1
B-2	406.4	5.017	0.25	0.500	Flat bottom	182.72	0.30	150.0	5.00	1.00	0.00	Based on A-1, $R_m/t=40$	
C-1	406.4	36.945	0.25	0.500	Flat bottom	182.72	0.30	150.0	5.00	1.00	27.00	Based on A-1, with pressure	Group 2
C-2	406.4	9.912	0.25	0.500	Flat bottom	182.72	0.30	150.0	5.00	1.00	6.75	Based on B-1, with pressure	
C-3	406.4	5.017	0.25	0.500	Flat bottom	182.72	0.30	150.0	5.00	1.00	3.38	Based on B-2, with pressure	

### I.3.6 Analysis Approach

This section describes the analysis approach taken by the five participating organizations. General-purpose FE codes, either ABAQUS® or MARC® were used by the participants.

### I.3.7 Geometry Models

The FE models were constructed either by shell and line-spring elements or 3-D solid elements. A typical model using shell and line-spring elements from Participant P1 is shown in Figure I.45 and Figure I.46. Only one quarter of the pipe was modeled due to symmetry conditions. The shell and line-spring elements were of the type S8R5 and LS3S per ABAQUS notation, respectively. There were ten equally-spaced line-spring elements covering the one-half crack front in the model. The 14 shell elements were geometrically-spaced around the circumference, having smaller elements in the region adjacent to the crack. The axial length of the quarter model was  $10D_m$ , where  $D_m$  is the mean diameter of the

pipe. A typical FE model using 3-D solid elements (C3D20 in ABAQUS) is shown in Figure I.47 and Figure I.48 from Participant P2. The crack area was modeled using a refined mesh with quarter-point-singularity elements at the crack tip. The 3-D solid element model for Problem A-2 from Participant P3 is shown in Figure I.49 and Figure I.50. The model was made to work with the MARC code.

### I.3.8 Loading

Bending loads were imposed on the pipe section by applying a rotation at the far end of the pipe through a kinematic coupling or by four-point bending. In the shell and line-spring element models of Participant P1, the nodes on the far end of the pipe were tied to a reference node through “\*KINEMATIC COUPLING” as provided in ABAQUS. The rotational degree of freedom applied to the reference node is then transferred to the end of the pipe through the kinematic coupling. The same coupling mechanism was used in the 3-D solid element

model of Participant P2. The far end of the pipe was sufficiently far from the cracked plane so there was no end effect at the crack of interest.

A four-point bending set up was used by Participant P3, as illustrated in Figure I.51. A similar four-point bending set up was also used by Participant P5.

In cases with internal pressure loading, the internal pressure and the associated axial load were applied first. The magnitude of the axial load represented the end cap load from the internal pressure. The bending loads or displacements were applied subsequently. There was no pressure applied to the crack face in the cases with internal pressure loading.

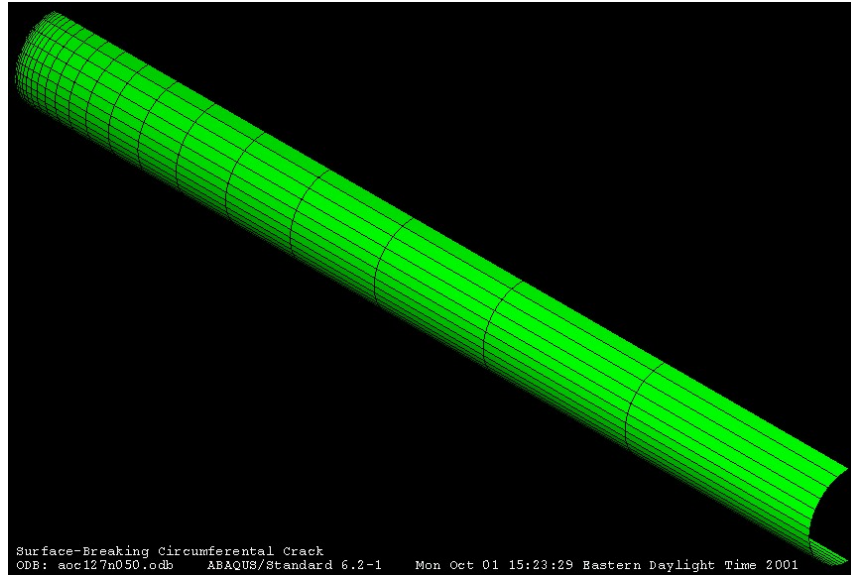


**Figure I.45** A typical model using shell and line-spring elements from Participant P1

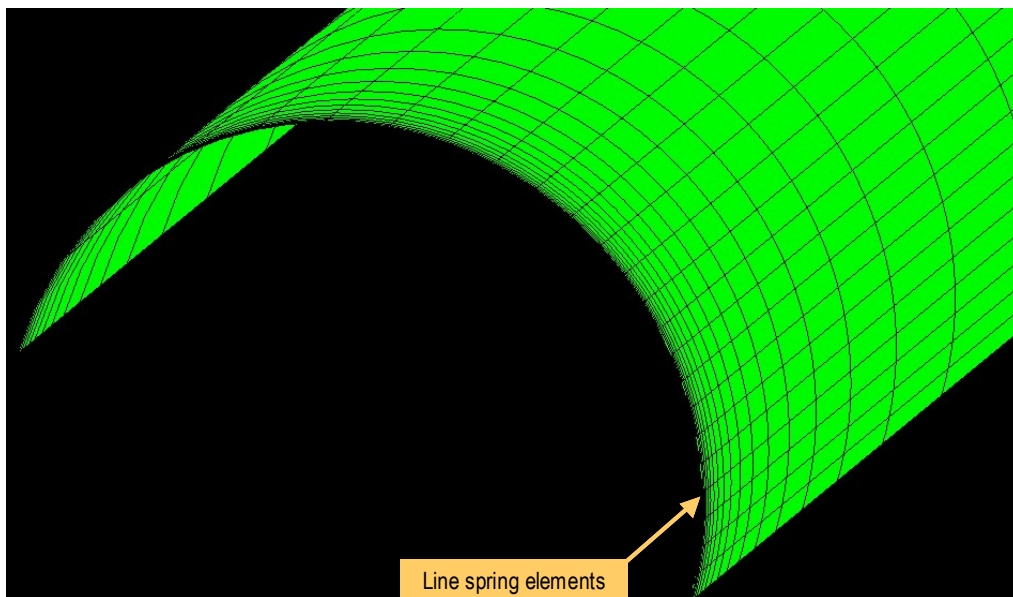


**Figure I.46** Focused view of the shell and line-spring model, looking at the cross-sectional plane containing the line-spring elements

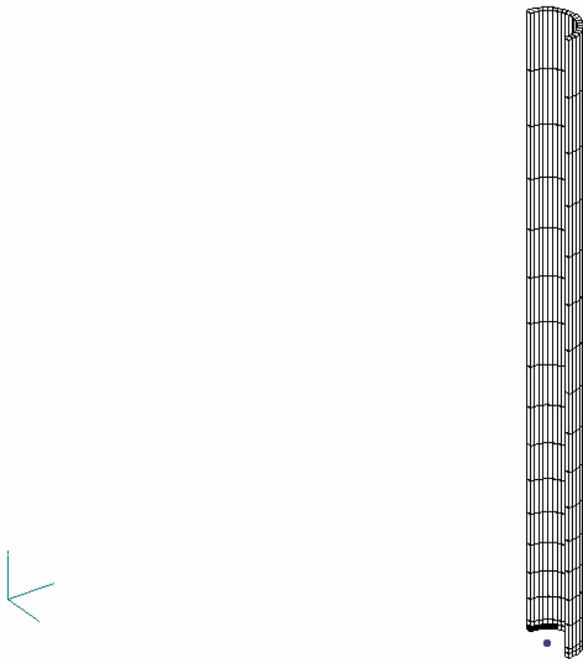


**Figure I.47 A typical 3-D solid element model from Participant P2**

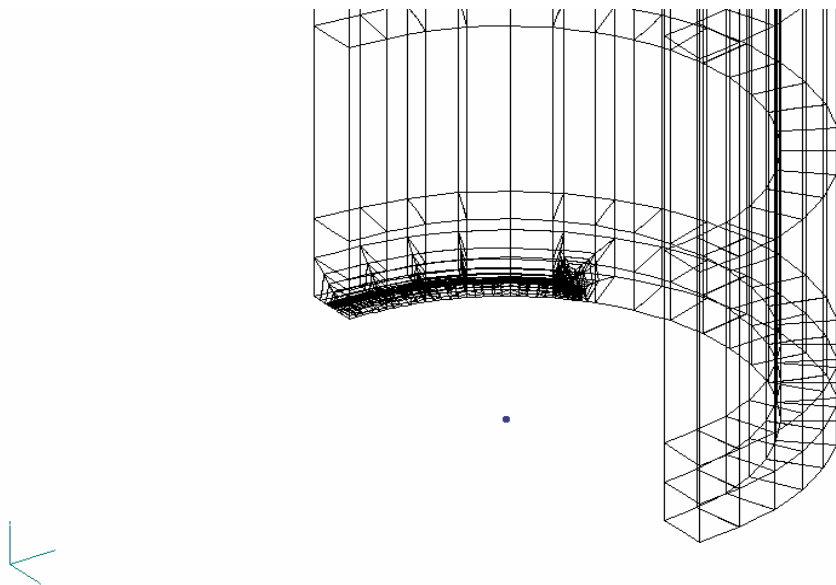
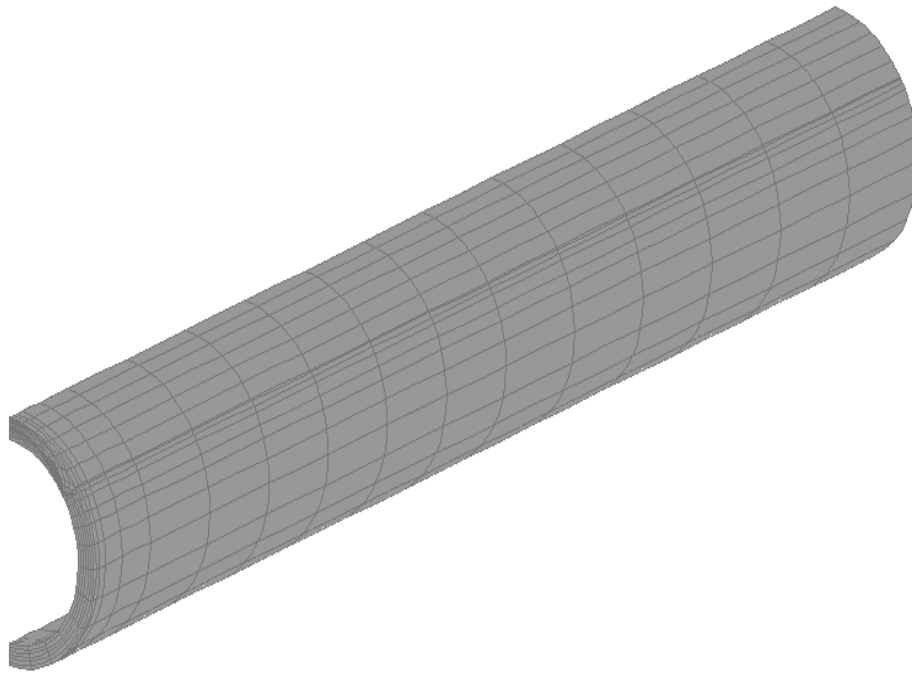


**Figure I.48 A focused view of the cracked region of a 3-D solid element model from Participant P2**

Inc: 0  
Time: 0.000e+00

MSC  
PATRAN



00a2



1

**Figure I.49 The 3-D solid element model of Problem A-2 from Participant P3**

Inc: 0  
Time: 0.000e+00

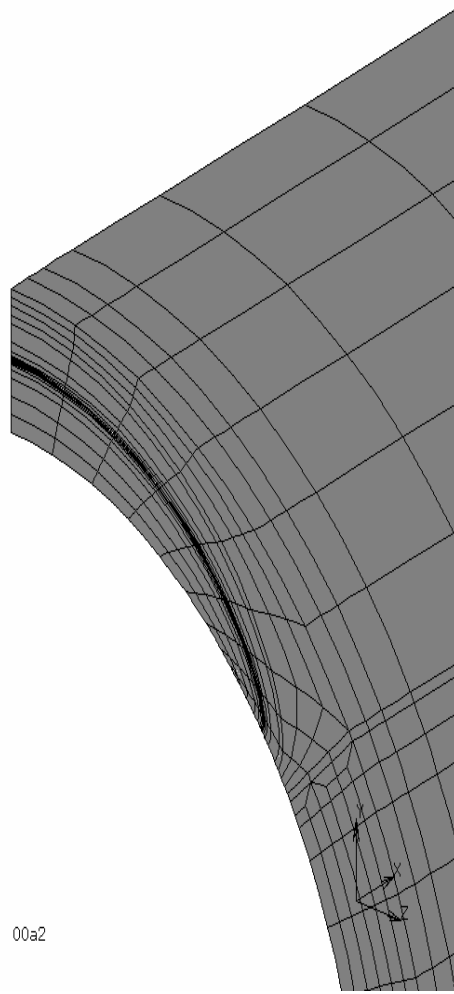
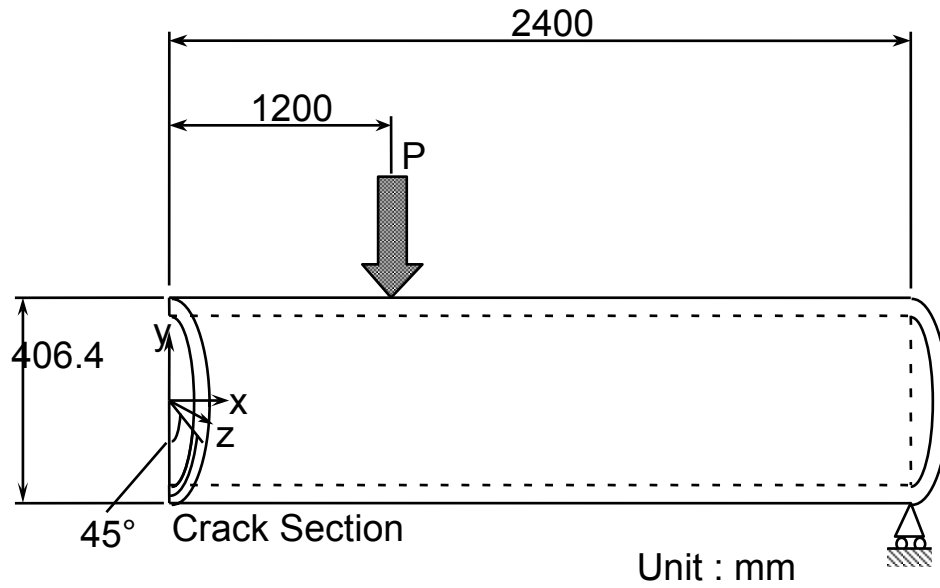
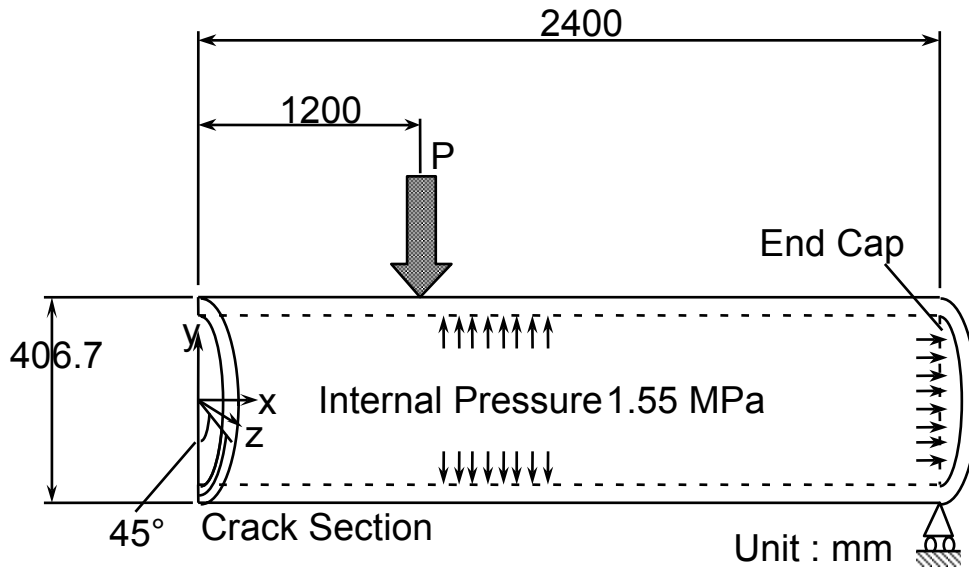


**Figure I.50 The focused view of the flawed area of the 3-D solid element model for Problem A-2 from Participant P3**



(a) Circumferentially Through-Wall-Cracked Pipe Subjected to 4-Point Bending (Cases A-1, B-1, B-2, and A-2)



(b) Circumferentially Through-Wall-Cracked Pipe Subjected to 4-Point Bending and Internal Pressure (Case A-3)

Figure 1 Loading Conditions

Figure I.51 Application of bending and internal pressure by Participant P3

### I.3.9 FE Procedure Formulation

A small-strain and small-displacement formulation was used by all participants except P3. Participant P3 employed large-strain (LS) and large displacement (LD) formulation for most of its analysis. For comparison, small-strain and small-displacement formulation was tried for some cases by Participant P3. The Ramberg-Osgood stress-strain relation of Equation I.1 conforms to the “\*DEFORMATION PLASTICITY” definition of ABAQUS. In the case of 3-D solid models, this definition can be used to precisely represent the power law hardening relationship of Equation I.1. In the case of shell and line-spring models, the “\*DEFORMATION PLASTICITY” definition does not work with the line-spring elements. Consequently, the material property has to be defined by the “\*ELASTIC” and “\*PLASTIC” cards in ABAQUS. The first line

of the “\*PLASTIC” card defines the plastic flow stress at zero plastic strain. In the case of Ramberg-Osgood stress-strain relation, the non-linearity starts at zero stress. Strictly speaking, the first line of the “\*PLASTIC” card would have zero plastic flow stress at zero plastic strain. However, ABAQUS does not allow zero plastic flow stress at zero plastic strain. Consequently, a small, but finite plastic flow stress, has to be given at zero plastic strain. The examination of the analysis results revealed that the magnitude of this finite plastic flow stress at zero plastic strain does not affect the  $J$  versus moment relation provided that this initial flow stress was less than one-third of reference yield stress, or  $\sigma_0$ . The analysis procedures and the associated FE codes of all participants are summarized in Table I.18. The blank cells of the table indicate that the corresponding information was not available to the authors.

**Table I.18 Summary of the analysis procedures of all participants**

Participant	Software		Element Type	Application of Bending load	Geometry/Strain Formulation
	Group	Code			
P1	1	ABAQUS	Shell and line-spring	Kinematic coupling	Small
P2	2	ABAQUS	3-D solid	Kinematic coupling	
P3	1	MARC	3-D solid	Four-point bending	Large and small
P4	2	ABAQUS	3-D solid		
P5	2	ABAQUS	Shell and line-spring	Four-point bending	

### I.3.10 Confirmation of the Analysis Procedures

To ensure the quality of the results, it was necessary to verify that the stress and strain state at the cracked plane was not affected by the boundary conditions applied at the far end of the model. The deformed shell and line-spring model from Participant P1, shown in Figure I.52, demonstrates that the cross-section of the pipe at the far end of the pipe remains circular, as if it were a cross section from a very long pipe. Figure I.53 shows that the axial stress has

the expected circumferential variation around the circumference of the pipe. This variation is independent of axial position for much of the model, except in the region close to the cracked plane. As expected, the axial stress redistributes in the cracked plane due to the reduced load carrying capability along the length of the surface crack. The deformation and stress patterns of Figure I.52 and Figure I.53 confirm that the stress and strain state in the cracked plane are free of end effects.

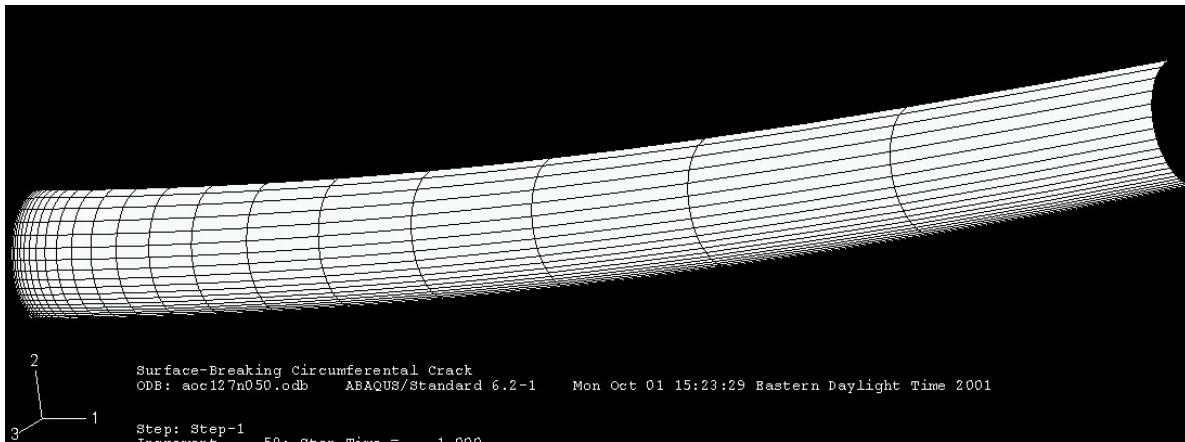


Figure I.52 A deformed shell and line-spring model from Participant P1

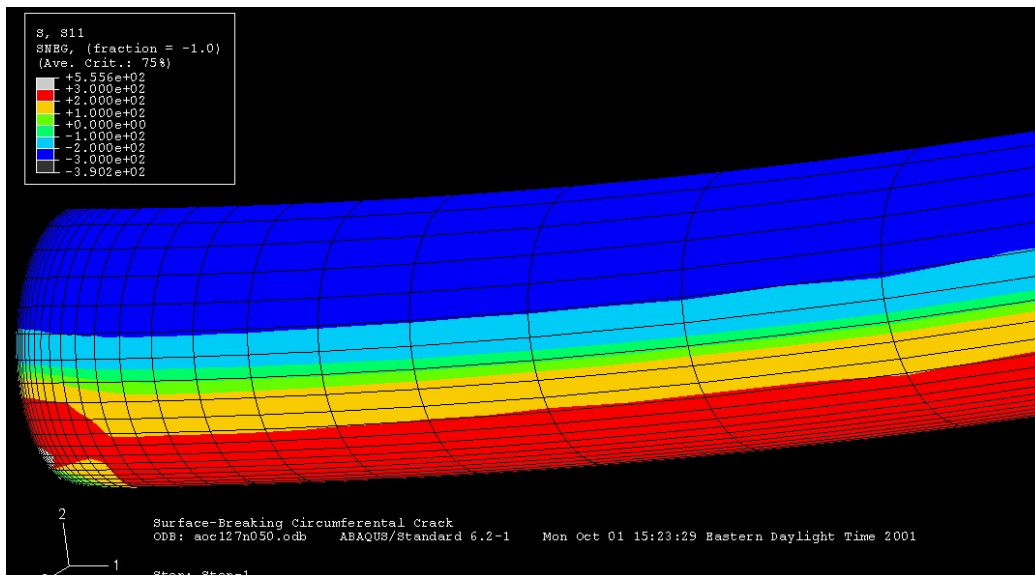


Figure I.53 Contours of axial stress of a deformed shell and line-spring model from Participant P1

### I.3.11 Comparison of $J$ versus Moment Relations

One of the objectives of this round robin was to provide some baseline  $J$  versus moment relations so the  $J$  estimation scheme can be expanded to higher  $R_m/t$  ratios than those in the current version of NRCPIPES. This section compares the  $J$  versus moment relations generated by all the participating organizations.

In the baseline Case A-1, the  $J$  versus moment relations have generally good agreement, see Figure I.54. At a  $J$  level of 500 N/mm, the maximum difference in bending moment

(between Participants P1 and P2) is approximately 11%. In Case A-2 of Figure I.55, the maximum difference in bending moment (between Participants P1 and P2) is reduced to approximately 8%. The only difference between Case A-1 and A-2 is the flaw shape. Case A-1 has flat-bottom flaw shape, while Case A-2 has semi-elliptical flaw shape. In the line-spring model, the flaw depth is defined as a function of the circumferential position of the nodes that are tied to the line-spring elements. For the flat-bottom flaws, the flaw depth in the entire flaw length covered by the line-spring elements was given as a constant. The sharp transition at the end of the flaw length could not be defined

precisely in the line-spring model. In the case of semi-elliptical flaw shape, the flaw depth was gradually transitioned to a zero depth. The line-spring model can define the gradual transition of

flaw depth more precisely. This may have contributed to the reduced difference in Case A-2.

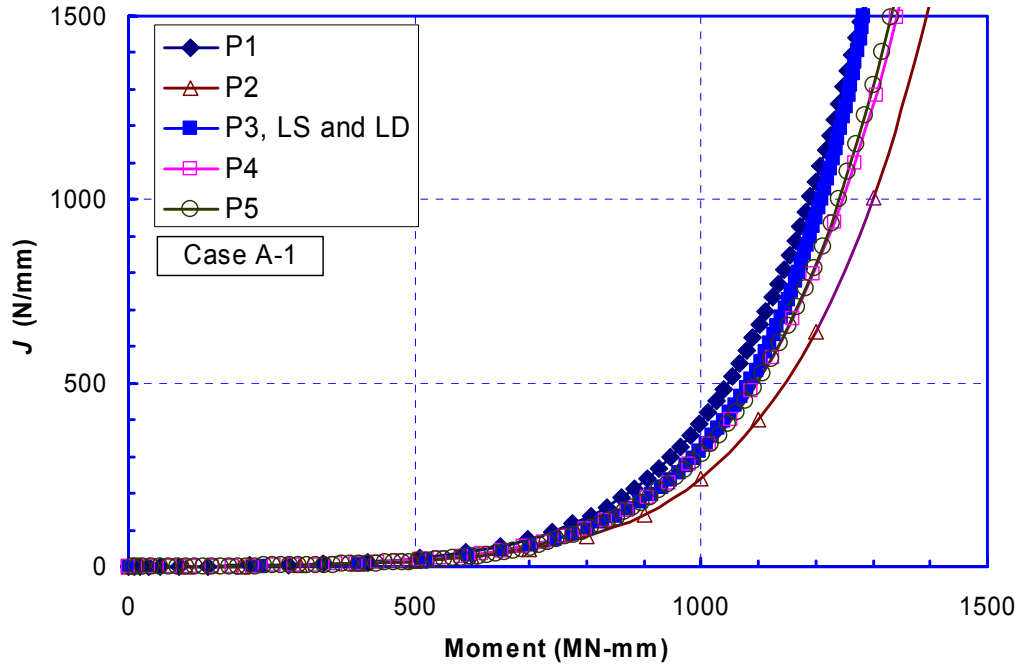


Figure I.54 The  $J$  versus moment relations of Case A-1. LS and LD stand for large strain and large displacement, respectively

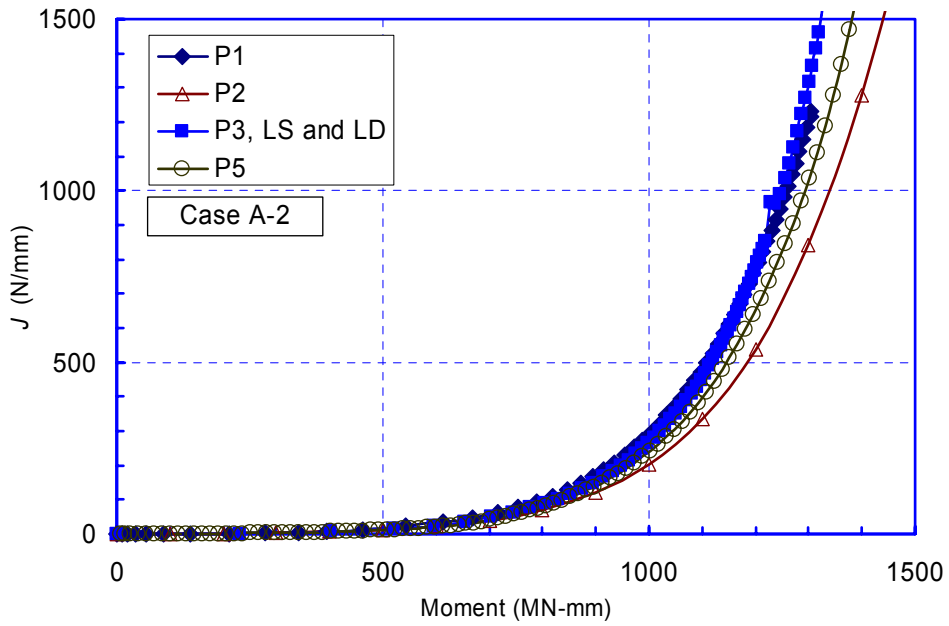


Figure I.55 The  $J$  versus moment relations of Case A-2

Case A-3 of Figure I.56 was set to simulate pipe Experiment 1.2.1.20. The  $R_m/t$  is much greater than Cases A-1 and A-2. Furthermore, there is a small internal pressure. The maximum moment difference at  $J=500$  N/mm is approximately 18%. The results of Participants P1, P2, and P3 are in one group, while the results of Participants P4 and P5 are in another group. This grouping is not consistent with the grouping of modeling approach (shell and line-spring versus 3-D solid elements). For instance, Participant P1 used shell and line-spring elements, while Participants P2 and P3 used 3-D solid elements. Furthermore, Participants P1 and P2 used a small-strain and small-displacement formulation, while P3 used a large-strain and large-displacement formulation. Yet the results of Participants P1, P2, and P3 are in the same group. Similarly, Participant P4 used 3-D solid elements, while Participant P5 used shell and line-spring elements. Yet the results of Participants P4 and P5 are in the same group.

bending moments. The large-strain and large-displacement formulation of Participant P3 captured the effect of cross section change of the pipe. This change eventually resulted in buckling of the pipe. Therefore there is an upper-bound limit of the bending moment, as reflected by the asymptotic increase of the  $J$  with little increase of bending moment.

The results of Participant P3 in Case B-2 demonstrate that the effect of buckling is more pronounced for pipes with large  $R_m/t$  as compared to Case B-1, see Figure I.58. The upper-bound moment was achieved at a relatively low  $J$  of approximately 300 N/mm in the analysis with large-strain and large-displacement formulation. Interestingly, the small-strain and small-displacement results of Participant P3 are closer to its own large-strain and large-displacement results, not the small-strain and small-displacement results of Participant P1.

In Case B-1 of Figure I.57, the results of Participants P1 and P3 are close until the large

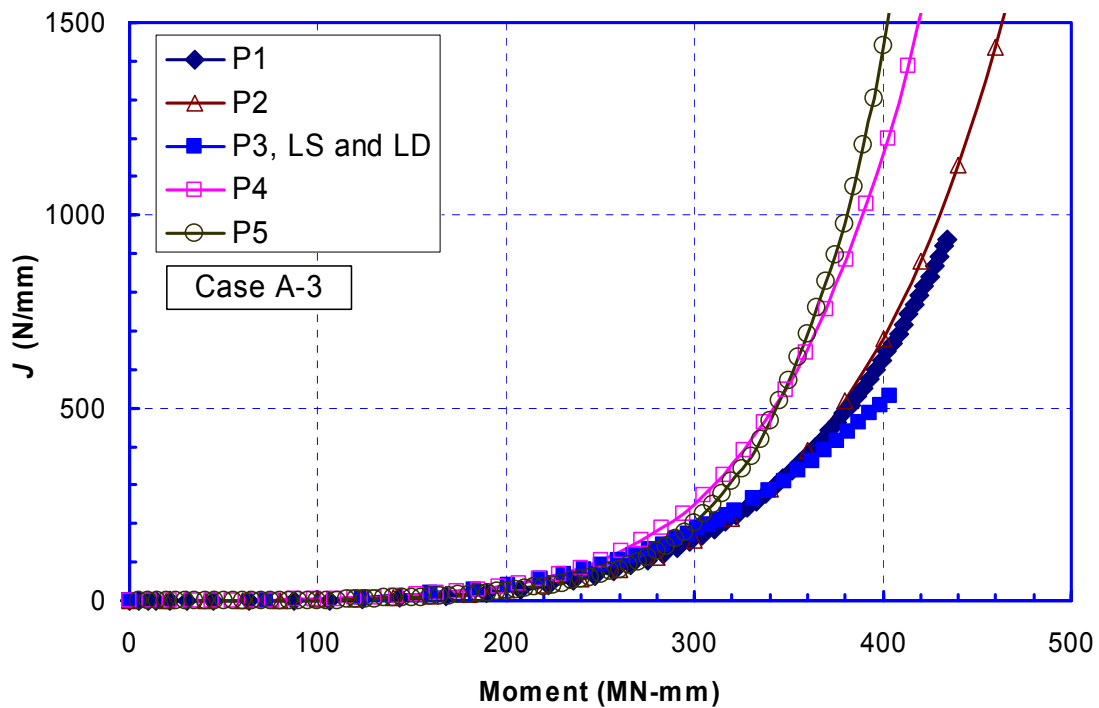


Figure I.56 The  $J$  versus moment relations of Case A-3

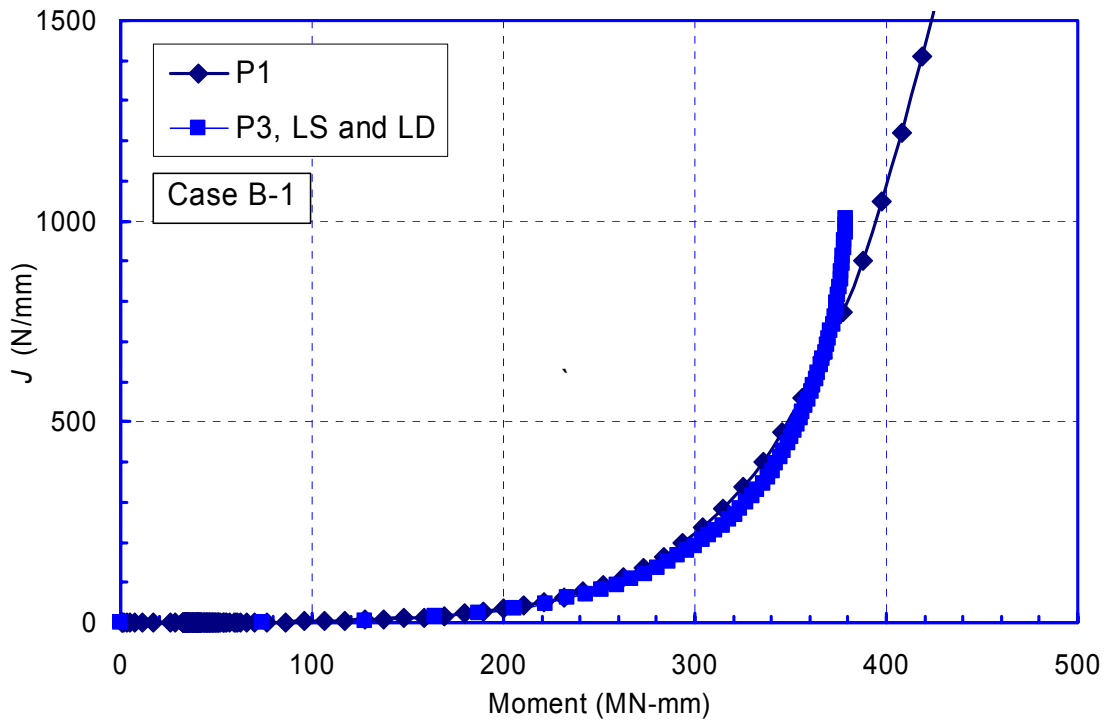


Figure I.57 The  $J$  versus moment relations of Case B-1

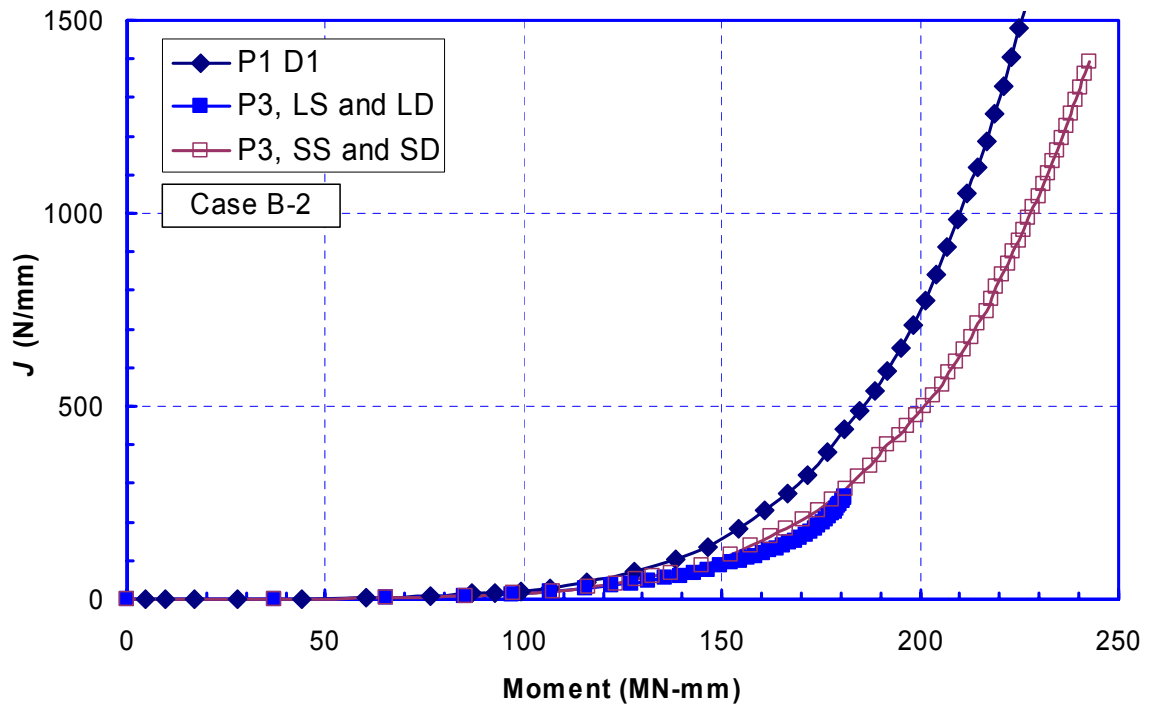


Figure I.58 The  $J$  versus moment relations of Case B-2. SS and SD stand for small strain and small displacement, respectively

Cases C-1, C-2, and C-3 were designed to examine the effects of  $R_m/t$  on the  $J$  versus moment relations with internal pressure. The difference in the  $J$  versus moment relations increases substantially with the increase of  $R_m/t$ , see Figures I.59, I.60, and I.61. The largest difference is in Case C-3 with an 80 percent spread in moment at the  $J$  value of 500 N/mm. In Cases C-1 and C2, the results are grouped by the types of FE models. For instance, the results of Participants P1 and P5 are in one group; both used shell and line-spring elements. The results of Participants P2 and P4 are in another group; both used 3-D solid elements. However, such grouping does not exist for Case C-3. The results of Participant P3 are particularly puzzling. The  $J$  versus moment curve does not have the asymptotically vertical trend as seen in Cases B-1 and B-2. Instead, the slope of the curve decreases with the increase of moment in the last few load increments. The Case C-3 results of Participant P3 are of large-strain and large-displacement formulation, the same as for Cases B-1 and B-2.

### I.3.12 Discussion of Results

The effects of modeling approaches were investigated further. The focus was on the difference between the shell and line-spring model versus the 3-D solid element model. The results of Participants P1 and P2 were the focus of this further investigation. To further simplify the comparison, elastic solutions were generated. The additional benefit of the elastic solution is that the results from open literature can be used for further validation.

The pipe geometry of Case A-1 was selected and first loaded in axial tension. The results of Participant P1, with either flat-bottom or semi-elliptical crack shape, are compared with those of Anderson (Ref. I.18) in Figure I.62. The solution of Anderson was derived using 3-D solid elements with semi-elliptical crack shape. The results of Participant P1 compare very well

with those of Anderson for the same crack shape. As expected, the  $J$  value of flat-bottom crack is higher than that of the semi-elliptical crack at the same load level.

Similar comparison was conducted for the 3-D solid element results of Participant P2, see Figure I.63. The first impression is that the difference between the flat-bottom and semi-elliptical crack shapes is much smaller than that from the shell and line-spring model. The agreement between the results of Participant P2 and those of Anderson is very good.

Appreciable difference is observed between the line-spring results of Participant P1 and that of Anderson under remote bending, see Figure I.64. Figure I.65 shows that the results of Participant P2 using 3-D solid elements are in better agreement with those of Anderson under the same loading condition. The comparison of Figure I.64 and Figure I.65 suggest that it is possible that the shell and line-spring model may overestimate the elastic  $J$ . The same conclusion cannot be drawn from the results of all cases listed in 17. In some of those cases, the shell and line-spring models provided higher  $J$  values than those of the 3-D solid models. In other cases, the opposite was true.

Using essentially the same analysis approach as Participant P1, Wang obtained elastic  $K$  solutions of internal circumferential cracks of various sizes (Ref. I.19). The line-spring solutions of semi-elliptical shape agreed well with the 3-D solid element solutions with semi-elliptical shape of Chapuloit (Ref. I.20), as shown in Figure I.66. The difference in  $J$  versus moment curves among the participating organizations cannot be attributed entirely to the difference in the use of FE elements. It may be deduced that the 3-D solid element solutions of Chapuloit are different from those of Anderson, although a direct comparison of those two solutions was not conducted in this round robin.

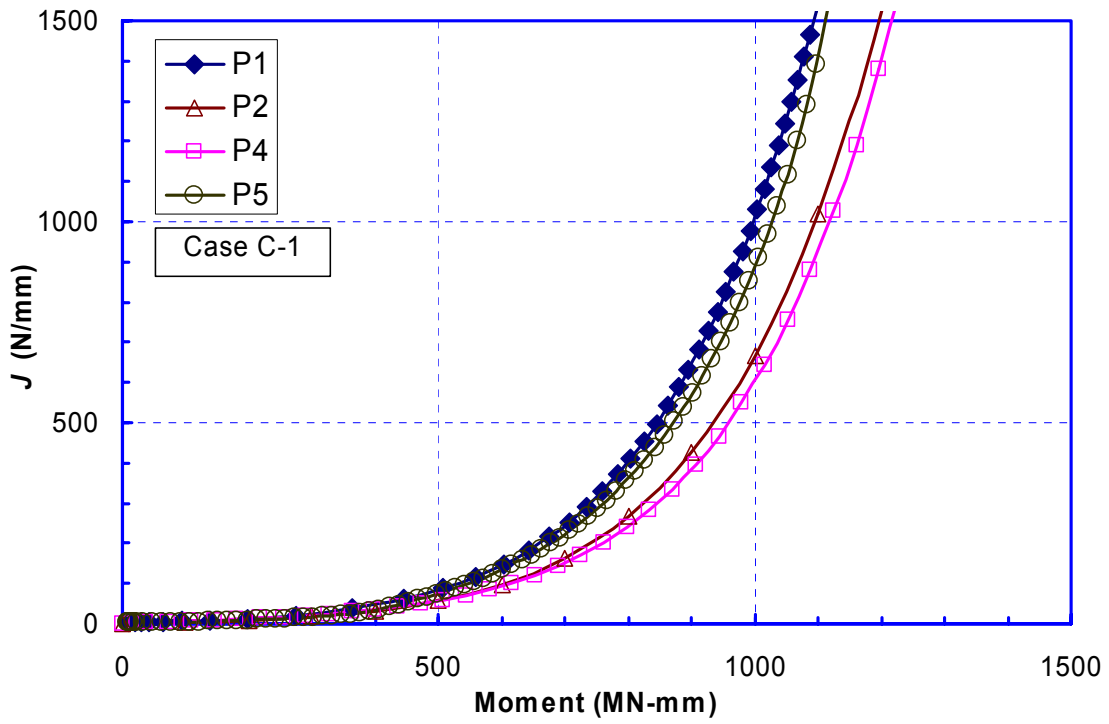


Figure I.59 The  $J$  versus moment relations of Case C-1

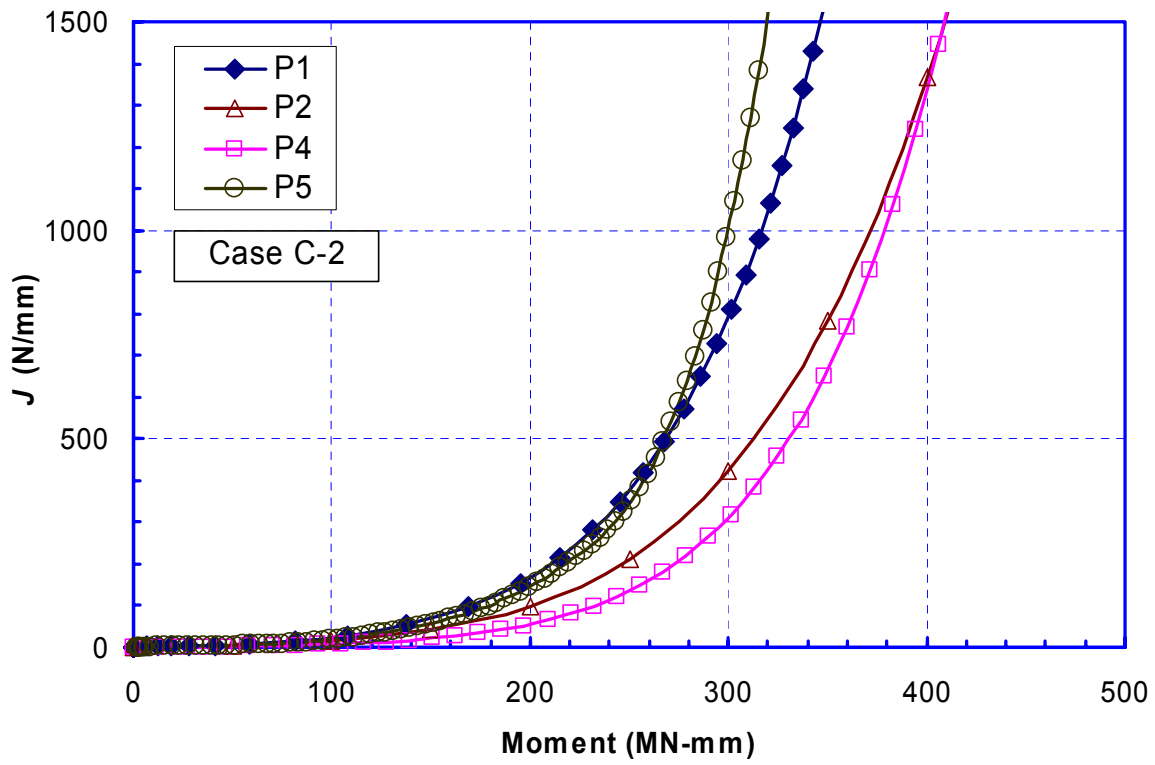


Figure I.60 The  $J$  versus moment relations of Case C-2

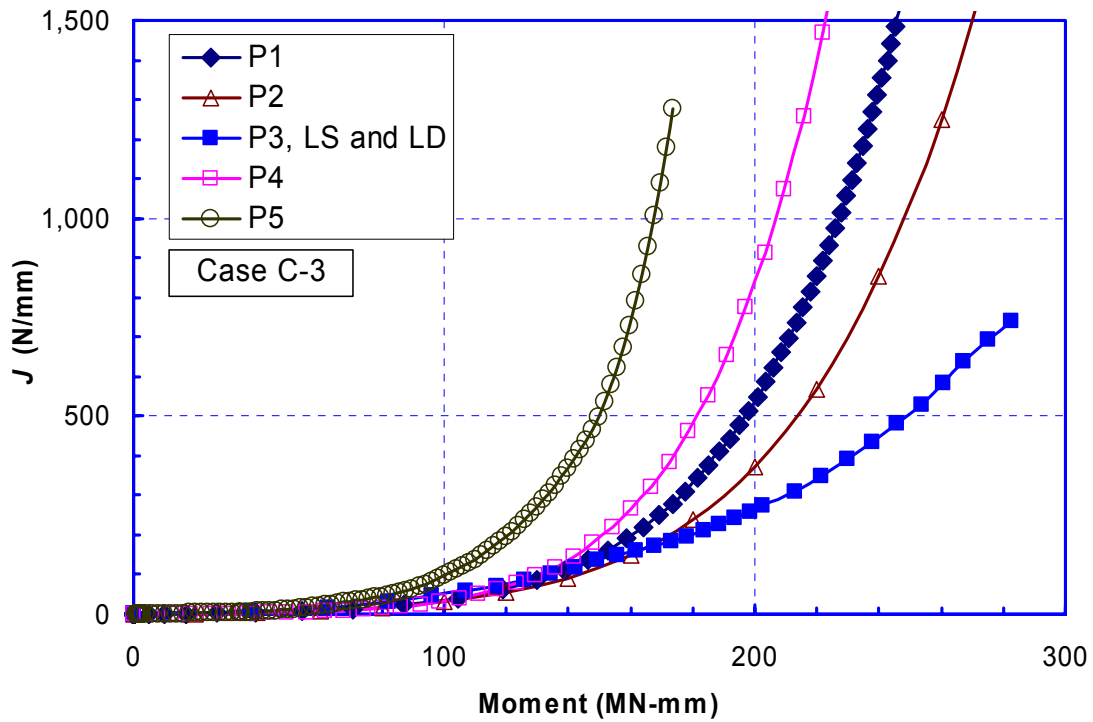


Figure I.61 The  $J$  versus moment relations of Case C-3

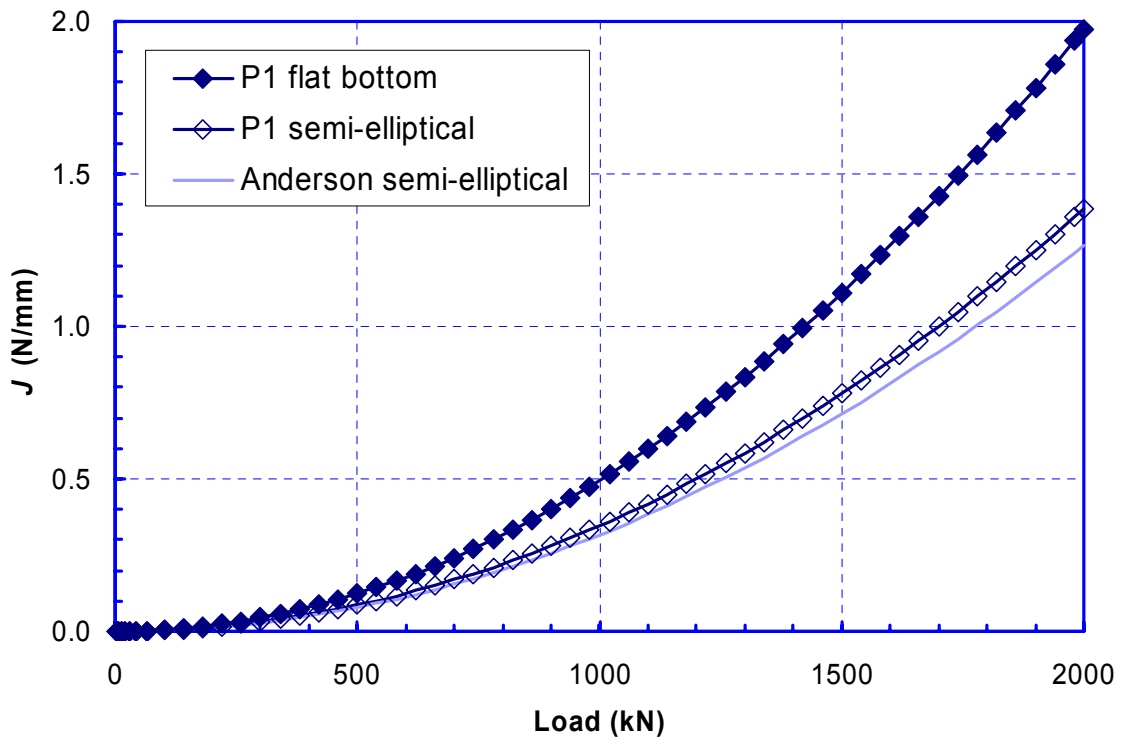


Figure I.62 Comparison of the line-spring results of Participant P1 with the 3-D solid element results of Anderson for a pipe section loaded in tension

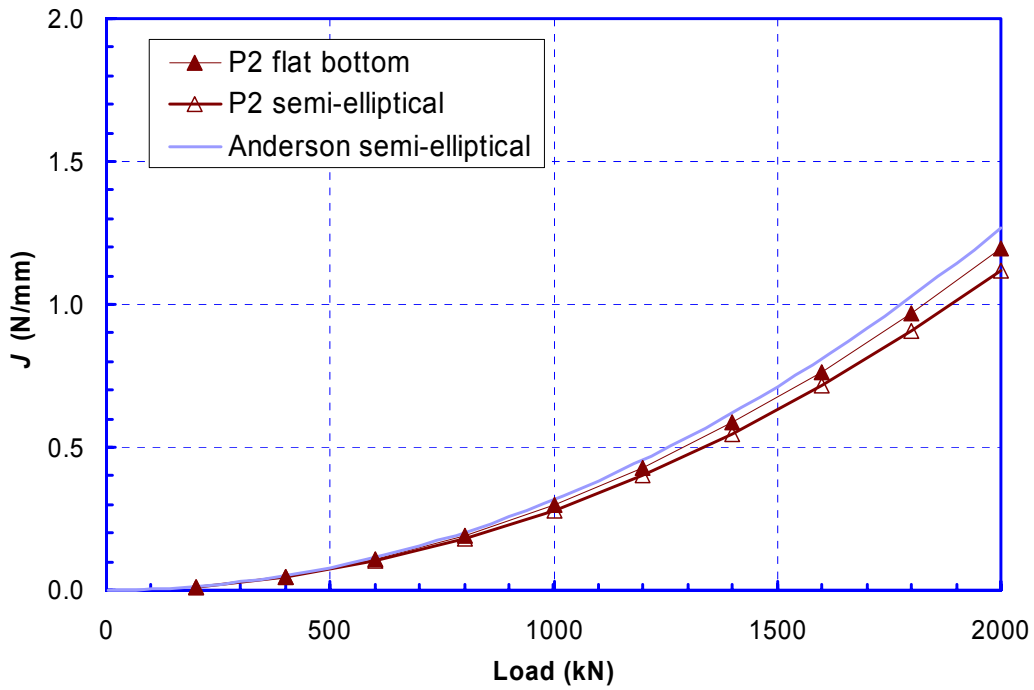


Figure I.63 Comparison of the 3-D solid element results of Participant P2 with the 3-D solid element results of Anderson for a pipe section loaded in tension

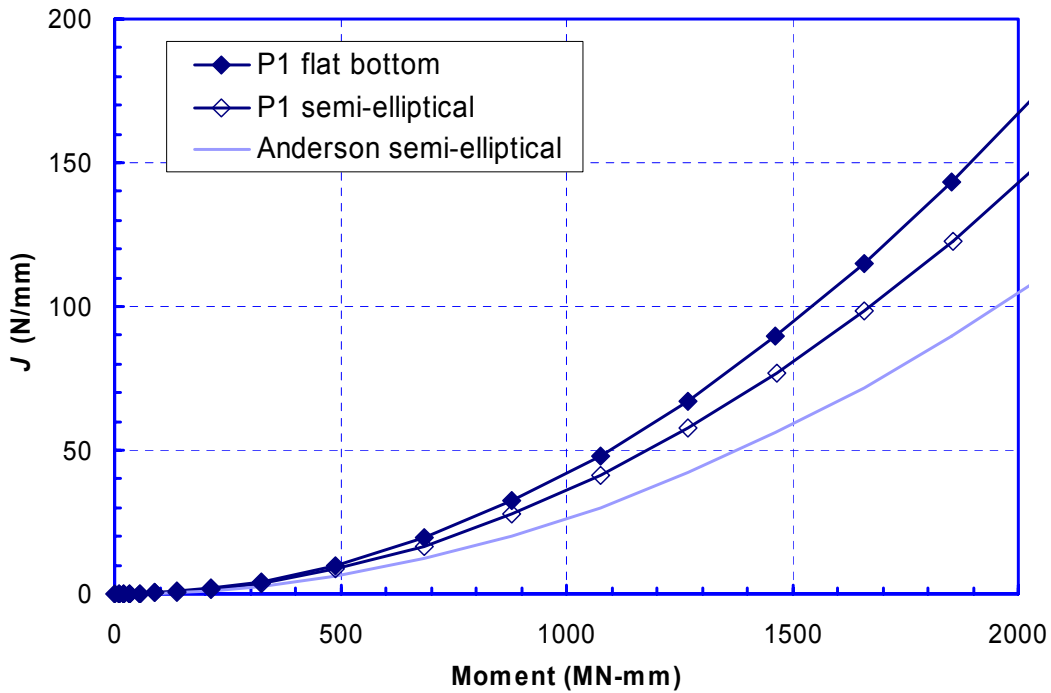


Figure I.64 Comparison of the line-spring results of Participant P1 with the 3-D solid element results of Anderson for a pipe section loaded in bending

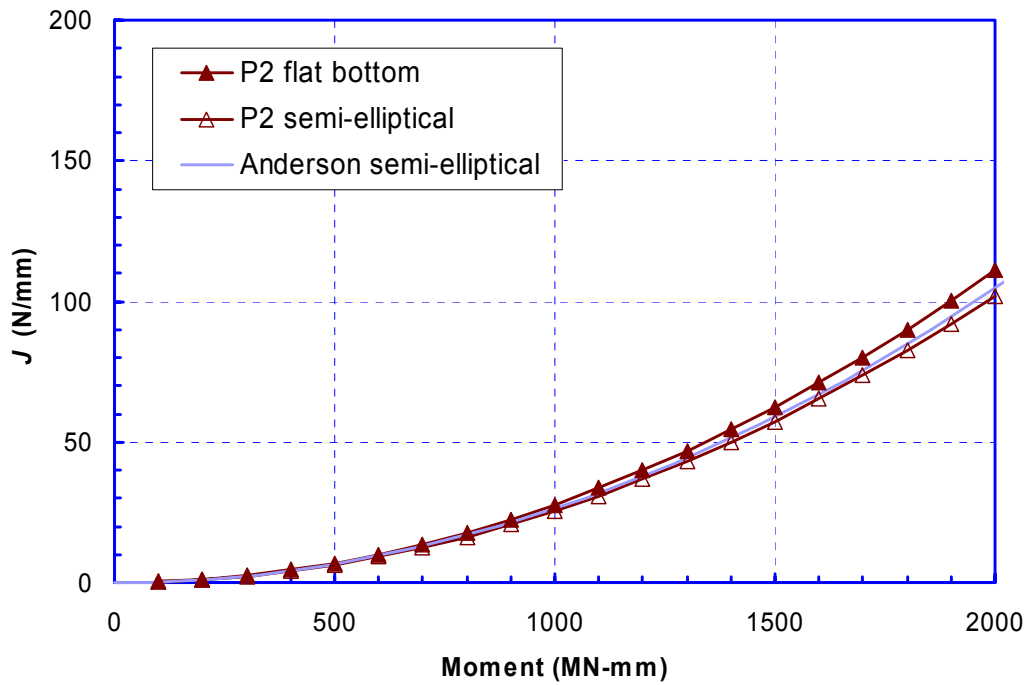


Figure I.65 Comparison of the 3-D solid element results of Participant P2 with the 3-D solid element results of Anderson for a pipe section loaded in bending

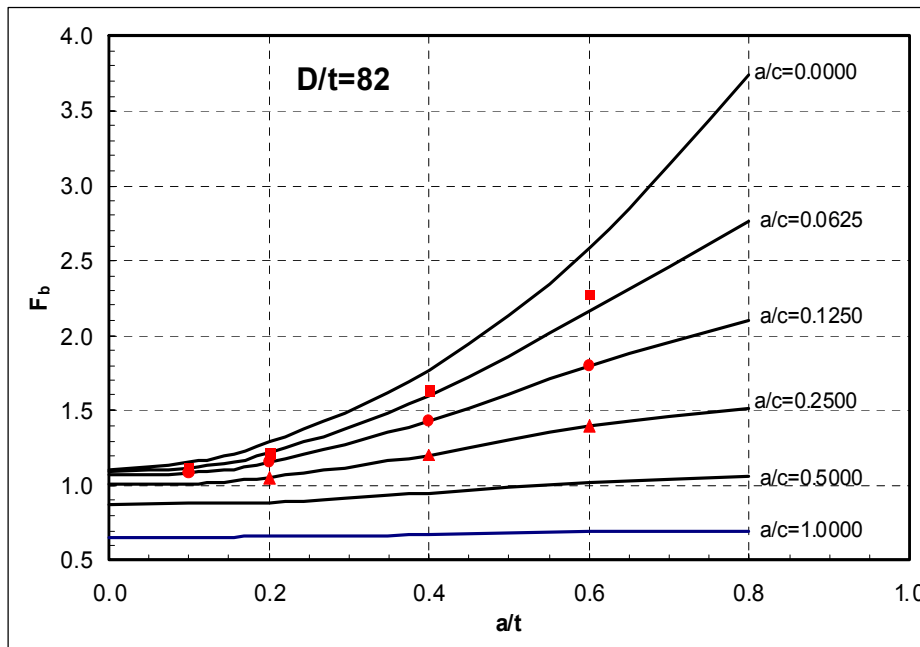


Figure I.66 Comparison of the normalized  $K$  solutions from the line-spring solution of Wang (Ref. I.19) with the 3-D solid element solution of Chapuloit (Ref. I.20). The lines are from Chapuloit; the symbols are from Wang

### I.3.13 Concluding Remarks

The differences among all participants in bending moment at the  $J$  level of interest in Cases A-1, A-2, B-1, B-2, and C-1 are typically less than 10 percent. Larger differences are observed in Cases A-3, C-2, and C-3. By comparison, the cases with internal pressure show larger differences than the cases without internal pressure. Although the use of shell and line-spring versus 3-D solid elements may cause some difference in the  $J$  versus moment relations, it cannot possibly be responsible for the large differences observed in some cases. Further investigation is needed to understand the causes of those large differences in some cases.

As indicated earlier, the possibility of local buckling at the surface crack location increases with the increase of  $R_m/t$  ratio. The local buckling reduces the load-carrying capability of the pipes. If the  $J$  estimation scheme were to extend to large  $R_m/t$  ratios, the effect of this local buckling should be considered in the FE analysis by using large-strain and large-displacement formulation. This work showed that sufficient accuracy could be obtained with the line-spring FE approach for the purpose of developing/validating an estimation scheme procedure. However, care should be taken in developing that approach for pipe with  $R/t$  of 40 or greater since local buckling at the crack may reduce the pipe's load-carrying capacity more than determined from using the small-strain formulation required for line-spring analyses. A separate effort for the BINP program involves comparing the FE line-spring results to different  $J$ -estimation schemes for the purpose of selecting or modifying one that gives consistent agreement with the FE analysis for the applied  $J$  versus moment behavior.

### I.4 REFERENCES

I.1 Ghadiali, N., Rahman, S., Choi, Y.H., and Wilkowski, G., "Deterministic and Probabilistic Evaluations for Uncertainty in Pipe Fracture Parameters in Leak-Before-Break and In-Service Flaw Evaluations," U.S. Nuclear Regulatory Commission, NUREG/CR-6443, 1996.

I.2 Rahman, S., Brust, F., Ghadiali, N., Choi, Y.H., Krishnaswamy, R., Moberg, F., Brickstad, B., and Wilkowski, G., "Refinement and Evaluation of Crack-Opening-Area Analyses Circumferential Through-Wall Cracks in Pipes for Circumferential Through-Wall Cracks in Pipes," U.S. Nuclear Regulatory Commission, NUREG/CR-6300, 1995.

I.3 Wilkowski, G. M., Ahmad, J., Barnes, C. R., Broek, D., Brust, F., Guerrieri, D., Kiefner, J., Kramer, G., Landow, M., Marschall, C. W., Maxey, W., Nakagaki, M., Papaspyropoulos, V., Pasupathi, V., and Scott, P., "Degraded Piping Program - Phase II Semiannual Report, October 1986-September 1987," NUREG/CR-4082, BMI-2120, Vol. 6, April, 1988.

I.4 Brickstad, B., "Swiss-Swede Analysis Program: Numerical Analyses of IPIRG Cracked Pipe Experiments with use of Non-Linear Fracture Mechanics," presented at 7th IPIRG-1 TAG meeting Nov. 1989.

I.5 Shimakawa, T., and Yagawa, G., "The Influences of Mesh Subdivisions on Nonlinear Fracture Analysis for Surface Cracked Structures," ASME PVP Vol. 167, pp. 7-14, July 1989.

I.6 Doi, H., and others, "Elasto-Plastic analysis of Pipe with Internal Circumferential Crack in Bending," ASME PVP Vol. 167, pp. 57-62, July 1989.

I.7 Takahashi, Y., and others, "Elastic-Plastic Fracture analysis of Surface Cracks in Pipe and Plates by three-Dimensional Finite Element Method," ASME PVP, Vol. 167, pp. 63-69, July 1989.

I.8 Miyoshi, T., and others, "Finite element Elastic-Plastic Analysis of Growth and Penetration of a Surface Crack," IJPVP, Vol. 33, 1988, pp 15-25.

I.9 Wilkowski, G. M., and others, "International Piping Integrity Research Group (IPIRG) Program," Program Final Report, NUREG/CR-

6233, Vol 4, June 1997, (pg 2-107).

I.10 Mohan, R., and others, "Development of a  $J$ -Estimation Scheme for Internal Circumferential and Axial Surface Cracks in Elbows," NUREG/CR-6445, BMI-2193, June 1996, see Section 3.0.

I.11 "NRCPIPES" *Windows Version 3.0 - User's Guide*, April 30, 1996, Battelle document to 2<sup>nd</sup> IPIRG group, Contract NRC-04-91-063.

I.12 Scott, P. M., and Ahmad, J., "Experimental and Analytical Assessment of Circumferentially Surface-Cracked Pipes Under Bending," NUREG/CR-4872, April 1987.

I.13 Krishnaswamy, P., Scott, P., Mohan, R., Rahman, S., Choi, Y. H., Brust F., Kilinski, T., Ghadiali, N., Marschall, C., and Wilkowski, G., "Fracture Behavior of Circumferential Short-Surface-Cracked Pipe," NUREG/CR-6298, November 1995.

I.14 Brust, F. W., "Approximate Methods for Fracture Analyses of Through-Wall Cracked Pipes," NRC Topical Report by Battelle Columbus Division, NUREG/CR-4853, February 1987.

I.15 Brust, F., Scott, P., Rahman, S., Ghadiali, N., Kilinski, T., Francini, R., Marschall, C., Muira, N., Krishnaswamy, P., and Wilkowski, G., "Assessment of Short Through-Wall Circumferential Cracks in Pipes - Experiments and Analyses," NUREG/CR-6235, April 1995.

I.16 Kurihara, R., and others, "Estimation of the Ductile Unstable Fracture of Pipe with a Circumferential Surface Crack Subjected to Bending," *Nuclear Engineering and Design*, Vol. 106, pp. 265-273, 1988.

I.17 Mohan, R., Wilkowski, G. M., Bass, B., and Bloom, J., "Finite Element Analyses to Determine the  $R/t$  Limits for ASME Code Case N-494 FAD Curve Procedure," ASME PVP Conference, PVP Volume 350, pp. 77-88, July 1997.

I.18 Anderson, T., Thorwald, G., Revelle, D.,

Lanaud, C., "Stress Intensity Solutions for Surface Cracks and Buried Cracks in Cylinders, Spheres, and Flat Plates," report to MPC, March 14, 2000.

I.19 Wang, Y.-Y., Rudland, D., and Crompton, J., "Development of Structural Integrity Assessment Procedures and Software for Girth-Welded Pipes and Welded Sleeve Assemblies," draft final report, PRCI PR-185-9831, April, 2001.

I.20 Chapulot, S., Lacire, M. H., and Le Delliou, P., "Stress Intensity Factors for Internal Circumferential Cracks in Tubes over a Wide Range of Radius over Thickness Ratios," PVP Vol. 365, ASME 1998, pp. 95-106.

**BIBLIOGRAPHIC DATA SHEET**

*(See instructions on the reverse)*

1. REPORT NUMBER  
*(Assigned by NRC, Add Vol., Supp., Rev.,  
and Addendum Numbers. if anv.)*

2. TITLE AND SUBTITLE

3. DATE REPORT PUBLISHED

MONTH

YEAR

4. FIN OR GRANT NUMBER

5. AUTHOR(S)

6. TYPE OF REPORT

7. PERIOD COVERED *(Inclusive Dates)*

8. PERFORMING ORGANIZATION - NAME AND ADDRESS *(If NRC, provide Division, Office or Region, U.S. Nuclear Regulatory Commission, and mailing address; if contractor, provide name and mailing address.)*

9. SPONSORING ORGANIZATION - NAME AND ADDRESS *(If NRC, type "Same as above"; if contractor, provide NRC Division, Office or Region, U.S. Nuclear Regulatory Commission, and mailing address.)*

10. SUPPLEMENTARY NOTES

11. ABSTRACT *(200 words or less)*

12. KEY WORDS/DESCRIPTORS *(List words or phrases that will assist researchers in locating the report.)*

13. AVAILABILITY STATEMENT

unlimited

14. SECURITY CLASSIFICATION

*(This Page)*

unclassified

*(This Report)*

unclassified

15. NUMBER OF PAGES

16. PRICE

